Copyright Undertaking

UNDERWATER WIRELESS COMMUNICATION SYSTEM

LO KING SHING

MPhil

The Hong Kong Polytechnic University

2025

The Hong Kong Polytechnic University

Department of Electrical and Electronic Engineering

Underwater Wireless Communication System

Lo King Shing

A thesis submitted in partial fulfillment of the requirements for
the degree of Master of Philosophy

August 2024

CERTIFICATE OF ORIGINALITY

I hereby declare that this thesis is my own work and that, to the best of my knowledge and belief, it reproduces no material previously published or written, nor material that has been accepted for the award of any other degree or diploma, except where due acknowledgement has been made in the text.

______________________ (Signed)

_____LO KING SHING___ (Name of student)

Dedicated

To my Families

Abstract

Underwater communication systems (UWC) have been a research focus since the mid-20th century, driven by the need for effective communication in underwater environments for applications such as environmental monitoring, underwater exploration, and defense operations. Among the various UWC methods, underwater radio frequency (UWRF) communication is significantly limited by high attenuation, making it impractical for further development. Consequently, researchers have turned their attention to underwater acoustic communication (UWAC) for long-range transmission and underwater optical communication (UWOC) for short/medium-range applications.

Recent advancements in UWAC have trended towards the use of Multiple Input Multiple Output (MIMO) technology to enhance data rates and communication reliability. However, conventional UWAC systems rely on transducers, which make MIMO configurations bulky and impractical. To address this issue, there is a strong motivation to investigate the integration of fiber acoustic sensing into underwater acoustic communication technology, which offers advantages such as small size, insulation, and resistance to electromagnetic interference. However, traditional fiber optic sensors with tunable narrow linewidth laser sources, such as FBG, interferometers, FP cavities, and micro resonance cavities, must be phase-locked to

achieve high sensitivity and stability. This requirement complicates the setup and makes the detected signal prone to distortion. It is essential to investigate alternative acoustic optical fiber-based detection techniques that provide high sensitivity and the ability for multiplexing.

On the other hand, light-emitting diode (LED)-based UWOC systems are preferred over laser diode (LD)-based systems due to their relaxed alignment requirements and auxiliary lighting capabilities. Nevertheless, LED-based systems encounter nonlinear distortion, with modulation nonlinearity of the LED playing a predominant role, resulting in substantial performance deterioration. Equalization algorithms, such as Volterra-based equalizers, are frequently adopted. However, the integration of the Volterra feedforward equalizer (VFFE) with the decision feedback equalizer (DFE), known as VDFE, remains susceptible to error propagation in the case of incorrect symbol decisions. As a result, it is essential to find alternative equalization techniques that can ensure good system performance.

In light of these challenges, this thesis focuses on a time-stretched self-coherent detection (TSSCD)-based underwater acoustic communication (UWAC) system for long-range acoustic signal transmission and an LED-based underwater optical communication (UWOC) system for medium-range transmission. The proposed schemes have been successfully demonstrated experimentally, and their performance has been evaluated. The 2.2-Mbps TSSCD-based UWAC system achieved a noise equivalent pressure (NEP) of 0.53 Pa/Hz^1/2 and applied amplitude modulation with the PAM-4 format on a sinusoidal ultrasonic signal with a frequency of 11 MHz. Additionally, a nonlinear weighted decision feedback equalizer (NWDFE) was introduced and demonstrated in a 520-Mbps PAM-4 blue-LED-based UWOC system for the first time, improving the data rate by approximately 9% while maintaining similar complexity compared to VFFE-DFE. The research study shall help to advance underwater communication technology.

Acknowledgements

How time flies; my two-year MPhil journey is about to come to an end. First and foremost, I would like to express my deepest gratitude to my supervisors, Prof. Lu Chao. His invaluable guidance, generous encouragement, and unwavering support have helped me overcome the difficulties encountered during my MPhil period. In particular, Prof. Lu's expertise and dedication have not only enriched my research in optical fiber communication and sensing but also inspired me to maintain my enthusiasm for life. I am profoundly grateful for his mentorship and the opportunities he has provided me throughout this journey. It is my great honor to be one of his students.

I would also like to extend my special thanks to Dr. Zhang Junwei and Dr. Li Yujia, who offered me unconditional assistance and provided insightful suggestions during my research process. Their valuable experience and critical thinking in the fields of optical communication and laser optics have significantly enhanced the quality of my research work.

My gratitude also extends to all my colleagues at the Photonic Research Institute at The Hong Kong Polytechnic University for their support during my MPhil period, especially Dr. Zheng Hua, Dr. Wu Xiong, Mr. Lu Liwang, Mr. Wang Jingchuan, and

Dr. Wang Yuyao. Additionally, I am thankful to all the people I met at PolyU, whose presence made my MPhil experience rich and diverse.

Finally, I would like to extend my heartfelt thanks to my parents, my girlfriend, and my best friends, whose encouragement and companionship have been a constant source of motivation. Their help has enabled me to overcome all the difficult times. Their support has been invaluable, especially during challenging times. I am grateful for their understanding, patience, and the countless moments of joy and laughter we have shared.

This degree has never made me regret my decision!

Table of Contents

List of Figures

List of Tables

Chapter 1

1. Introduction

1.1 Overview

Communication is a fundamental aspect of human interaction. To advance societal benefits, scientists have developed various technologies to enable wireless communication. While terrestrial wireless communication technologies have achieved significant maturity, attention has now turned toward underwater communication as an emerging frontier. The understanding of acoustic wave properties in marine environments has opened a new chapter in underwater wireless communication (UWC) research and development. Given that oceans cover approximately 70% of the Earth's surface, there has been a marked increase in human activities within marine domains, including oceanographic research, climate monitoring, underwater resource exploration, and tactical surveillance. The ability to achieve a high speed, long range and reliable communication is essential for many applications, however, underwater communication channel is very complicate and RF signal used for terrestrial wireless communication will be strongly attenuated.

This means new communication technology has to be developed for underwater environment.

As of 2021, the global market for UWC is projected to expand from USD 918 million to USD 1689.9 million by 2028 [1]. The advent of the 'smart ocean' concept and the underwater Internet of Things (IoT) necessitates UWC systems with more advanced technical specifications. To advance UWC systems, it is imperative to address the unique challenges posed by the aquatic environment. One of the primary obstacles is signal attenuation, which diminishes communication range. Initially, radio waves, prevalent in terrestrial communication, were considered for UWC; however, they are rapidly absorbed by seawater, leading to high signal attenuation. As an alternative, acoustic waves have been utilized, which are relatively less affected by attenuation due to absorption, scattering, and reflections [2]. However, the inherently low data rates of UWC systems, attributed to the low carrier frequency of acoustic signals, limit the volume of transmittable information and, consequently, the scope of potential applications and services [3]. In contrast, optical communication technology offers substantially higher bandwidth and data transmission rates, meeting the demand for high-speed underwater data transfer more effectively than radio or acoustic methods, albeit with a constrained transmission range. Additionally, the presence of noise from marine life, surface waves, and anthropogenic activities can interfere with communication signals, diminishing the signal-to-noise ratio and complicating the achievement of reliable communication [2]. Hence, to surmount the challenges associated with UWC, researchers have employed a diverse array of strategies, encompassing radio frequency, acoustic, and optical communication techniques. Each method offers unique advantages and confronts specific limitations within the complex marine environment.

1.1.1 Underwater Radio Frequency Communication (UWRFC) system

The exploration of electromagnetic waves (EM), particularly radio frequency (RF), for underwater wireless communication (UWC) dates back to the early 20th century. However, the pronounced attenuation of RF signals in water, especially at higher frequencies, has historically constrained their utility in subaqueous settings [4]. RF carriers, while not entirely unfeasible, are generally limited to covering only short ranges within aquatic environments. For underwater propagation, the frequency spectrum of EM waves has been reported to be exceedingly low, ranging from 30 to 300 Hz, primarily for military applications [5]. Researchers have concentrated on the ultra-low-frequency (ULF) band to achieve seawater penetration of up to several tens of meters with minimal attenuation, a technique that has found application in submarine communication and navigation [6]. Despite these efforts, underwater wireless radio frequency (UWRF) communication still grapples with signal fading and rapid attenuation over short distances, particularly in turbid water conditions. The combination of high costs and low data transmission rates has impeded the widespread adoption and cost-effectiveness of this approach.

1.1.2 Development of Underwater Acoustic Communication (UWAC) system

The underwater wireless acoustic communication (UWAC) systems typically consist of transducers and hydrophones that convert electrical signals into sound waves and vice versa, enabling the transmission and reception of messages [7]. Traditional acoustic wireless carriers propagate over long distances at a low speed of approximately 1500m/s and have a limited data rate [8]. The acoustic waves propagation speed can be influenced by channel impairment in general, while the speed increases tremendously due to fluctuation of the temperature and salinity of the water [4]. The UWAC has received significant interest in view of its ability to propagate signals over long distances in the underwater medium [6], [9], and work in non-line-of-sight and without affect by water quality. However, the underwater acoustic channel presents unique challenges such as multipath propagation, Doppler shifts, and high and variable delay spreads, which significantly affect the performance of communication systems. Diamant and Lampe [10] provide a comprehensive review of low probability of detection (LPD) in UWAC. They highlight the main challenges in designing UWAC LPD systems, including the various approaches for transmission, reception, and interception of LPD signals. The discussion on advantages and weaknesses of these approaches sets the stage for understanding the intricate balance between stealth and reliability in underwater communication. Improving signal detection accuracy under the influence of the Doppler shift is critical in UWAC. Diamant et al. [11] propose a novel method for Doppler shift estimation using two chirp signals. Their approach demonstrates significant improvements in accuracy over benchmark methods, especially at near-Nyquist baseband sampling rates. This advancement in dealing with Doppler shifts is pivotal for enhancing the robustness of communication in dynamic underwater environments. Zhang et al. [12] introduce a modulation recognition system for UWAC signals that leverages higher-order cumulants and deep learning. This system can achieve blind recognition of received signals under non-cooperative conditions, addressing the non-linearity and time-variance of underwater channels. This work underscores the potential of integrating advanced signal processing and machine learning techniques in UWAC. The application of low-density parity-check (LDPC) codes for improved image transmission in UWAC is explored by Das et al. [13]. Their study demonstrates how LDPC codes can compensate for the variable nature of underwater noise, contributing to the reliability and efficiency of image transmission over UWAC channels. Xing et al. [14] present an analysis of a wireless powered communication network (WPCN)-based UWAC system. They investigate system performance in terms of average bit error rate, outage probability, and achievable information rate in a frequency-selective sparse channel and non-white noise environment. This research highlights the importance of energy-efficient solutions for enhancing the sustainability and reliability of UWAC systems. Jiang and Diamant [15] address the challenge of sparse channel estimation for long-range UWAC. By combining block subspace pursuit and distributed subspace pursuit algorithms, they exploit the block structure of the channel, which plays a crucial role in optimizing long-range communication strategies in UWAC. Lu et al. [16] propose a spatial-digital joint self-interference cancellation (SDSIC) method to address the challenge of in-band full-duplex (IBFD) UWAC. Their approach, including an improved wideband constant-beamwidth beamformer, tackles the issue of direction and array-dependent interference, thereby enabling more efficient duplex communication in underwater environments. Especially in the modulation and digital signal processing schemes, 2019, Chen et al. [17] proposed a multi-carrier chaos modulation scheme for UWAC, which combines code-shifted differential chaos shift keying (CS-DCSK) with orthogonal frequency division multiplexing (OFDM). The proposed system demonstrated good robustness under time-varying underwater acoustic channels. Similarly, in 2020, a new UWAC scheme that combines Doppler-resilient orthogonal signal division multiplexing (D-OSDM) and multiple-input–multiple-output (MIMO) signaling, which showed promising results in terms of bit error rate performance [18]. In the parallel development, Xi et al. [19]

proposed a hybrid frequency-time domain turbo equalizer (FTD-TEQ) for UWAC, which not only performed better but also had lower computational complexity than traditional methods. After two years, multiple hyperbolic frequency-modulated (MHFM) signals and binary phase-coded hyperbolic frequency-modulated (BHFM) signals for UWAC system is demonstrated, which provided better performance, higher timing estimation accuracy under challenging conditions, and enhancing system performance in high multipath environments respectively [20], [21]. Last year, Kumar [22] suggested a new optimized least square sparse (OLSS) channel estimation algorithm for UWAC, which outperformed conventional models in terms of symbol error rate (SER), bit error rate (BER), mean square error (MSE), and peak signal-to-noise ratio (PSNR). Although, the above works can effectively mitigate the challenges by developing new modulation schemes, signal processing techniques, and channel estimation algorithms, the focal point is still based on improving the software, instead of upgrading the receiver part. However, an important element in such systems is an effective acoustic signal detector that enables highly sensitive acoustic signal detection and realization of system of detector array for MIMO signal detection. It is important to investigate technologies that can realize such detectors.

1.1.3 Development of Underwater Optical Communication (UWOC) system

Due to the limited data rate and bandwidth of UWAC and UWRF, an alternative approach using optical signal has become a significant and reliable wireless carrier candidate for digital signaling in underwater [23]. Researchers recognized that visible light, particularly in the blue-green region of the spectrum (450-530 nm), experiences minimal absorption in seawater compared to other wavelengths [24]. Without the limitation of data rate and bandwidth, light emitting diodes (LEDs) with lower attenuation were proposed for implementation in the UWOC systems to provide a transmission data rate of up to several tens of Mbps [25-29]. Although UWOC systems require line-of-sight, and limited transmission range [30], it has low latency, and low energy consumption. In UWOC systems, transmitters typically use laser diodes (LDs) or light-emitting diodes (LEDs). Laser-based UWOC systems having the advantages of relatively long communication distance the communication capacity. Recently, the research in laser-based UWOC systems approaching to use large active area detector like photomultiplier tube [31,32], scintillating-fiber-based photoreceiver [33], and large-photovoltaic cells [34] to overcome the issue of misalignment. On the contrary, LEDs offer a more robust solution for short to medium distances with better misalignment tolerance. LED-based UWOC research has made significant progress in terms of data rates, transmission distances, and practicality, as evidenced by references [35-40]. Previous studies have succeeded in the application of UWOC in the challenging environment. A UWOC sea trial achieved data rates of 158-Mbps in the daytime and 205-Mbps in the nighttime over a transmission distance of 10 meters in harbor water [35]. Another cost-effective real-time UWOC system using a field-programmable gate array (FPGA) achieved a data rate of 25-Mbps over 10 meters in an underwater channel [36]. Significant advances in LED-based UWOC systems using equal gain combined with an integrated PIN array reception and developing a GaN-based five-primary-color LED for UWOC system respectively [37], [38]. However, in addition to the limited modulation bandwidth causing linear inter-symbol interference (ISI), LED-based UWOC system also suffers from nonlinear distortion, resulting in a degradation of the signal-to-noise ratio (SNR) at the receiver side. The nonlinear distortion in UWOC system can be attributed to various components, including the modulation nonlinearity of LED, electrical amplifier, and square-law detection of photoreceiver (PD), among which the modulation nonlinearity of LED plays a predominant role [41], [42]. The presence of nonlinear distortion can have significant detrimental effects, particularly when advanced modulation formats such as pulse amplitude modulation (PAM) [41], [42], carrierless amplitude phase (CAP) modulation [43], and orthogonal frequency division multiplexing (OFDM) [44] are employed.

In the pursuit of enhancing the performance and reach of UWOC systems, researchers have focused on developing nonlinear equalization algorithms. These algorithms are designed to minimize interference and aid in signal recovery. The types of nonlinear equalizers include Decision Feedback Equalizers (DFE), Maximum Likelihood Sequence Estimation (MLSE), Neural Network Equalizers, and Sparse Nonlinear Equalizers. With advances in deep learning, Neural Network Equalizers have become particularly popular for addressing complex nonlinear issues. Since 2018, significant progress has been made in applying nonlinear equalizers in UWOC. In 2018, a study [45] presented an UWOC system that used a 450 nm gallium nitride (GaN) laser and adaptive bit power loading for discrete multitone (DMT). This system achieved a data rate of 7.33 Gb/s at a depth of 15 meters, with an error rate below the 7% threshold for hard decision forward error correction (FEC), demonstrating the positive effect of nonlinear equalizers on increasing system capacity. Also in 2018, Zhang's team [46] explored the use of post-nonlinear equalizers in UWOC, confirming their ability to compensate for distortions and enhance signal quality. In 2019, a sparse nonlinear equalizer that reduced computational demands while maintaining high performance, providing a new option for UWOC system design is introduced [47]. Moving into 2021, research in this area continued to advance. A comprehensive survey [48] reviewed UWOC systems, with a focus on the use and performance of nonlinear equalizers. The survey indicated that nonlinear equalizers can effectively improve data transmission rates and signal quality. Following this, Wang and his college [49] demonstrated a UWOC system capable of 200 meters at 500 Mbps, using a sparse nonlinear equalizer, further confirming their potential to enhance system performance.

Additionally, the use of neural network-based post-equalization methods [50] in underwater visible light communication has shown important progress. This approach, powered by deep learning, effectively compensates for nonlinear distortions, improving system performance. In May of the same year, Zhang and Liu et al. [51] discussed how nonlinear equalizers can increase the speed of UWOC systems when considering advanced modulation formats, highlighting the importance of coordinating the design of nonlinear equalizers with modulation formats to boost system performance. In July, Wu et al. [52] proposed a low-complexity frequency-domain nonlinear equalizer that improved UWOC system performance and reduced computational complexity. In August, Chen et al. [53] achieved 90-meter/660 Mbps underwater wireless optical communication by using an interleaved single-carrier frequency division multiplexing (I-SC-FDM) scheme with a sparse weight-initiated DNN equalizer, demonstrating the effectiveness of neural networks in handling complex nonlinear problems. Among the various approaches, the Volterra series-based model is a popular choice for its ability to provide a detailed representation of nonlinear behavior [54-58]. The use of Volterra series is favored because it captures the interactions between input signals and system responses, offering a detailed way to model and correct for signal distortions caused by nonlinear effects.

1.2 Comparison of different UWC systems

The UWC is mainly evaluated by the following parameters:

1) Attenuation: the reduction in signal strength as it travels through water.
2) Data rate: the speed of transmitting signal.
3) Latency: the time delay between sending a signal and receiving it.
4) Bandwidth: the capacity for transmitting data can be sent within a given time.
5) Transmission distance: the maximum distance that the signal can be reached.
6) Size: the portability and convenience of the communication system.

Among different UWC systems that have been developed over the past decades, there are varies of technical impediment UWC systems. Table 1. shows the comparison among different UWC systems. Table 2. shows the advantages and disadvantages among different UWC systems. It summarized that for both UWAC and UWOC systems are more desirable than UWRF systems, considering that it lacks neither a high data rate nor a long-distance transmission and suffering from high attenuation which can be solved by either UWAC or UWOC. Therefore, it is possible to achieve a better UWC by further improving UWAC and UWOC. For non-line-of-sight and long transmission distance situation, UWAC systems can be applied, while UWOC utilized for high data-rate and shorter transmission distance.

Table 1. Comparison among different UWC systems.

	UWRF	UWAC	UWOC
Attenuation	3.5-5 dB/m	0.1-4 dB/m	0.24-11 dB/m
Speed	$\approx 2.255\text{x}10^8$ m/s	1500m/s	$\approx 2.255\text{x}10^8$ m/s
Data rate	bps-kbps	kbps	Gbps
Latency	Moderate	High	Low
Distance	Up to ≈ 10 meters	Up to kms	≈ 10-100 meters
Bandwidth	≈ MHz	< 1 kHz (1000 km) ≈ 1 kHz (1-10 km) ≈ 100 kHz (<100 m)	10-150 MHz
Frequency band	3-30 kHz	10-15 kHz	10^{12} -10^{15} Hz
Transmission power	Few mW to hundreds of Watts	Tens of Watts (typical value)	Few Watts
Antenna size	A few km	0.1 m	0.1 m

Table 2. Advantages and disadvantages of different UWC.

	Advantages	Disadvantages
UWRF		➢ Very strong attenuation ➢ High cost ➢ High power consumption ➢ Short transmission range
UWAC	➢ Long transmission range ➢ Work in non-line-of-sight ➢ Not affected by water quality	➢ Limited bandwidth ➢ High latency
UWOC	➢ High bandwidth ➢ Low latency ➢ Low energy consumption	➢ Limited transmission range ➢ Work in line-of-sight

1.3 Motivation

The objectives of research conducted in this thesis are focuses on UWAC and UWOC systems for long range and middle range signal transmission respectively. In terms of long transmission range, UWAC utilizing polymer fiber (PF) with time-stretched self-coherent detection (TSSCD) technology can minimized the size, improve the portability and sensitivity. It may offers significant advantages when used with the multi-input multi-output (MIMO) technology in order to overcome its disadvantages that have been mentioned. For middle transmission range, UWOC system adopted linear or non-linear equalizers are straightforward and low-cost to migrate the non-linear effect from the system. Conventional hard-decision equalizers are often used for compensating nonlinear distortion, but suffering from error propagation. Making use of compressed sigmoid nonlinear function approach into a non-linear equalizer, which can limit the avoid channel feedback, and error propagation , while maintaining the complexity. More specifically, the thesis explores as follow.

1.3.1 Innovation of using TSSCD with PF in UWAC system

To overcome the limited bandwidth problem in UWAC systems, MIMO is a possible solution [60]. For example, in [61], it demonstrates a method to convert two-hop MIMO-OFDM relay channels into virtual SISO-OFDM direct links using the SVD technique. It introduces an iterative AFSA algorithm to optimize power allocation in these virtual links. The approach considers channel conditions measured in CNR and jointly assigns subcarriers and relay nodes to maximize capacity. In [62], they focus on multi-user underwater acoustic communication using massive MIMO-OFDM-based OTFS systems. The performance assessment for a 4-user scenario was conducted within a simulated 1 km vertically-oriented time-varying underwater acoustic channel. Nevertheless, massive MIMO system require compact and highly sensitive detector array with a centralized processing unit. Traditional passive sonar-based scheme is not the best choice for the MIMO system since the hydrophone are bulky, and connection to a central processing unit are also inconvenient with highly cost. Hence, fiber-optic ultrasonic sensors have attracted considerable attention due to their immunity to electromagnetic interference and small volume.

Recently, the optical detection methods of the ultrasound wave have attracted much attentions [63], due to its inherent large bandwidth and high sensitivity. It is very suitable for the underwater environment due to its compact size, insulativity and anti-electromagnetic interference. One of the most frequently-used optical methods is achieved by injecting a tunable narrow-linewidth laser source into the linear region of the transmission or reflection spectra of various high-Q factor components, such as the FBG [64], interferometer [65], FP cavity [66] and micro resonance cavity [67]. However, the low-frequency fluctuation in the water makes the lasing wavelength easily deviated from the linear region of the ultrasonic detector, resulting in the distortion of the detected signal and instability of the detection sensitivity. Thus, additional servo-locked setups are also necessary [68-71]. On the other hand, the dynamical ranges of the detector also limited by the linear works. Guan et al. has proposed one kind of birefringence short-cavity fiber laser to achieve the highly-sensitive ultrasonic detection by the demodulating the frequency of the beating signal between two polarization modes, which provides an excellent method to integrate the ultrasonic detector and light source [72, 73]. However, the fine grating writing technology has to be carefully explored, which is critical to avoid the unstable laser operation, such as the self-pulse phenomenon and multimode competition.

In order to overcome the disadvantages, we can demodulate the ultrasonic signal from the complete dynamical transmission spectra of the detectors affected by the ultrasound wave. Thus, other wideband light sources, such as the electro-optical dual-comb source with a large repetition rate difference and digital frequency comb are also injected into the detector to achieve the ultrasonic detection, which needs complex high-speed electrical modulation modules [74, 75]. The time-stretched swept laser is achieved by utilizing the dispersive medium to stretch the femtosecond optical pulse from mode-locked lasers in the time domain, which has been widely used in the fast spectroscope and imaging [76-78]. The large frequency chirp of the stretched pulse causes the frequency sweeping process. Thus, the sweeping rate of such laser source can reach 100 MHz order, which is completely determined by the repetition rate of the mode-locked laser [79, 80]. Due to the time-frequency mapping of the time-stretched fast swept source, the dynamical transmission spectra of the detector can be effectively captured, which is used to record the ultrasonic signal with a sampling rate equaling sweeping rate. Due to the Nyquist law, the detection bandwidth of the ultrasonic signal is determined by half the swept rate, which reaches tens-of-Megahertz. Because of the wide spectral properties of the light source, we need not lock the linear work region of the detector to achieve a stable detection sensitivity and avoid the distortion of the detection signal. Moreover, the femtosecond mode-locked laser is one kind of typical high-coherence wideband light, also resulting in the high-coherence of the swept source, which is helpful for compressing the noise floor of the detection system.

1.3.2 Contribution of using equalizer to migrate the nonlinearity in UWOC system

Underwater wireless optical communication (UWOC) is emerging as a viable alternative with its inherent advantages, including enhanced communication secrecy, low power consumption, and access to a large unlicensed bandwidth [81-83] as middle range transmission. In contrast to laser diodes (LDs) that are extensively utilized in long-reach underwater wireless optical communication (UWOC) systems, which demand stringent alignment, light-emitting diodes (LEDs) emerge as a more fitting option for scenarios necessitating a broad field of view (FOV), lenient alignment, and supplementary illumination. This preference stems from the inherent attributes of LEDs, such as their wide divergence angle and compatibility with natural illumination [84]. As a result, LEDs are deemed the optimal light source for practical UWOC system applications that target moderate data rates. Nevertheless, the bandwidth of commercially available and cost-effective blue and green LEDs is confined to a few megahertz, attributable to their significant junction capacitance and extended recombination lifetime [85]. Beyond the bandwidth constraint, LED-based UWOC systems also confront nonlinear distortion, which significantly degrades transmission performance. The nonlinear distortion in the UWOC system can be attributed to various components, including the modulation nonlinearity of LEDs, electrical amplifiers, and photoreceivers (PDs), among which the modulation nonlinearity of LED plays a predominant role [41], [42].

However, in addition to the limited modulation bandwidth causing linear inter-symbol interference (ISI), LED-based UWOC system also suffers from nonlinear distortion, resulting in a degradation of the signal-to-noise ratio (SNR) at the receiver side. The nonlinear distortion in UWOC system can be attributed to various components, including the modulation nonlinearity of LED, electrical amplifier, and square-law detection of photoreceiver (PD), among which the modulation nonlinearity of LED plays a predominant role [41], [42]. The presence of nonlinear distortion can have significant detrimental effects, particularly when advanced modulation formats such as pulse amplitude modulation (PAM) [41], [42], carrierless amplitude phase (CAP) modulation [43], and orthogonal frequency division multiplexing (OFDM) [44] are employed. One of the most widely adopted approaches for compensating nonlinear distortion in LED-based UWOC systems is to utilize 2nd-order/3rd-order Volterra feedforward equalizer (VFFE) [86], owing to its capability in modeling the intricate time-dispersive nonlinear channel response. Moreover, compared with 2nd-order/3rd-order VFFEs, the integration of VFFE and decision feedback equalizer (DFE), known as VFFE-DFE, can significantly enhance the transmission performance in bandwidth-limited LED-based VLC [41] and UWOC [42] systems. However, the VFFE-DFE is susceptible to error propagation in the case of wrong decisions. To avoid error propagation, the DFE can be relocated to the transmitter side named THP (THP) [87], which has been employed in LED-based bandwidth-limited UWOC transmission over a 1.2 m water tank [88]. Nevertheless, THP suffers from a pre-coding loss and necessitates accurate channel feedback [87]. Recently, linear and nonlinear weighted decision feedback equalizers (WDFEs) that integrate an improved rule based on a compressed sigmoid nonlinear function have been introduced. These advancements aim to curb error propagation and eliminate channel feedback in PAM-4 based optical fiber communication systems [89], [90]. Compared to traditional linear and nonlinear DFEs, these novel WDFEs have demonstrated substantial enhancements in transmission performance. Therefore, the concept of WDFEs would be able to make enhance e the performance of LED-based UWOC system.

1.4 Organization of the thesis

This thesis is divided into four chapters, organized as follows:

Chapter 1 summarizes the demand and challenges of underwater communication (UWC) and reviews research in underwater radio frequency (UWRF), acoustic (UWAC), and optical communication (UWOC) systems, highlighting the research motivation.

Chapter 2 overviews the principles of time-stretched self-coherent detection (TSSCD) and presents the development and experimental validation of a UWAC system using a time-stretched swept laser and a PF detector. The system achieves high sensitivity and low noise equivalent pressure (NEP), successfully transmitting PAM-4 signals at 2.2 Mbps, demonstrating good amplitude isolation and stability for the next generation of UWAC system.

Chapter 3 introduces a novel LED-based UWOC system using a Nonlinear Weighted Decision Feedback Equalizer (NWDFE). Combining a Volterra Finite

Impulse Response Filter (VFFE) and a Weighted Decision Feedback Equalizer (WDFE), the NWDFE effectively reduces distortions, improving data rates by 9% compared to VFFE-DFE, achieving 520 Mbps with similar complexity. This chapter highlights the NWDFE's success in enhancing UWOC system performance.

Chapter 4 summarizes the research findings and discusses potential future work.

Chapter 2

Underwater Wireless Acoustic Communication using polymer fiber based on the time-stretched self-coherent detection

Chapter 2 introduces the sensing principle based on coherent detection using a Mach-Zehnder Interferometer structure. Subsequently, the principle of a time-stretched self-coherence detection system with high speed and high coherence is presented. This scheme forms the foundation of the research works presented in this thesis. Finally, the ultrasound signal is recovered using the proposed technique and demonstrated experimentally with PAM-4 in order to achieve a data rate of 2.2 Mbps.

2.1 Principle of sensing based on coherent detection with Mach-Zehnder Interferometer structure

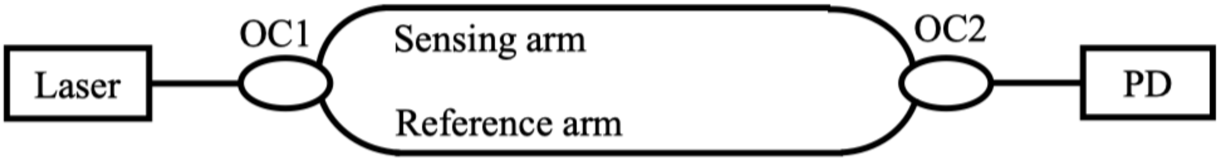

Fig. 1. The basic structure of the single Mach-Zehnder interferometer. OC: optical coupler; PD: photodetector.

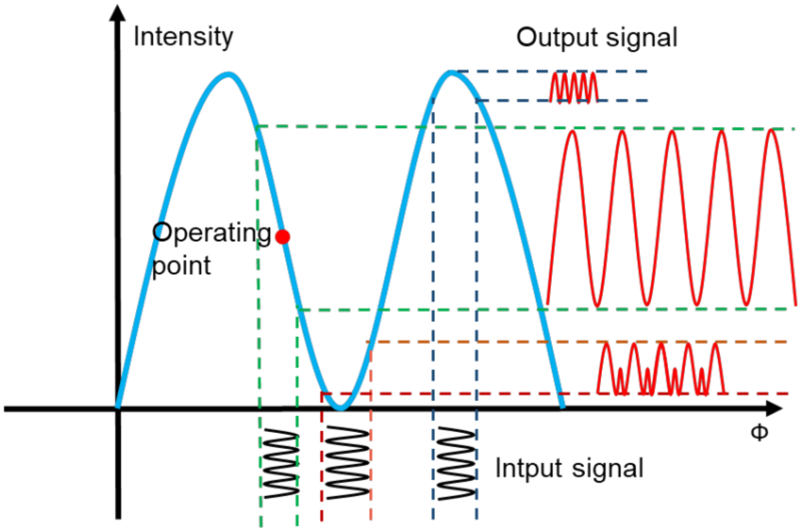

Fig. 1. Schematic diagram of demodulation results under different initial phases.

As depicted in Fig. 1, a tunable narrow-linewidth laser serves as the light source, emitting single-frequency laser light. Subsequently, the laser light passes through a fiber-based Mach-Zehnder interferometer (MZI) structure, where it is detected by a photodiode (PD) and subsequently converted into an electrical signal. This electrical signal is then stored and displayed by an oscilloscope. During ultrasonic detection, the interference spectrum experiences periodic drift due to the influence of ultrasonic pressure. Consequently, the intensity of the input single-frequency laser light fluctuates in accordance with the drift of the interference spectrum shown as Fig. 2. The frequency of the intensity fluctuations on the oscilloscope aligns with the ultrasonic frequency, and the peak-to-peak value of the signal is directly proportional to the sound pressure.

$$I = I_1 + I_2 + 2\sqrt{I_1 I_2}\cos(\frac{4\pi \mathrm{n}_{eff} L}{\lambda} + \phi_0) \tag{1}$$

In the provided formula, I_1 and I_2 denote the light intensities of the two modes participating in the interference. φ0 represents the initial phase of the interfering light, n_{eff} is the effective refractive index of the optical fiber, λ denotes the wavelength of the light, and l represents the interference length of the MZI structure. The sensing sensitivity of the fiber-based MZI structure, denoted as SMZI, can be defined as the ratio of the change in transmitted light intensity to the change in interference length. By differentiating the aforementioned formula, we obtain:

$$\phi = \frac{4\pi n L}{\lambda} + \phi_0 \tag{2}$$

$$S_{MZI} = \frac{dI}{dL} = -\frac{8\pi n\sqrt{I_1 I_2}}{\lambda}\sin(\phi) \tag{3}$$

From the sensitivity calculation formula, it can be determined that when φ = (2m+1)$\boldsymbol{\pi}$/2 (m is a positive integer), the sensing sensitivity of the fiber-based MZI structure is maximized. This point is designated as the quadrature working point (Quadrature point, Q point). When an ultrasonic wave is applied to the MZI structure, the interference light intensity can be expressed as:

$$I = I_1 + I_2 + 2\sqrt{I_1 I_2}\cos(\phi + \Delta\phi) \tag{4}$$

In the above formula, $\Delta\varphi$ represents the phase change induced by the ultrasonic wave. Assuming the ultrasonic wave possesses a frequency of ω_u and the change in the interference length of the MZI structure caused by sound pressure is ΔL, then $\Delta\varphi$ can be shown as:

$$\Delta\phi = \frac{4\pi n \Delta L}{\lambda}\sin(\omega_u t) \tag{5}$$

Since the electronic oscilloscope uses AC coupling, the DC component is removed, leaving only the AC component. The change in light intensity can be expressed as:

$$I_{AC} = 2\sqrt{I_1 I_2}\cos[\phi + \frac{4\pi n \Delta L}{\lambda}\sin(\omega_u t)] \tag{6}$$

Figure 2.7 illustrates the phase relationship between the Q point and the interference spectrum of the MZI structure. When an ultrasonic wave interacts with the MZI structure, the initial phase is set to φ = (2m+1)$\boldsymbol{\pi}$ /2 (m is a positive integer), corresponding to the quadrature working point. This configuration results in a weak ultrasonic signal causing a larger AC response output, indicating the highest Q point sensitivity, as depicted by the blue line in the figure. However, selecting other points, such as near the wave peaks and troughs, not only reduces the sensitivity but also introduces signal distortion. Consequently, when demodulating ultrasonic signals, it is crucial to lock the wavelength of the single-frequency laser output generated by the laser at the Q point. For fiber-based MZI structures, the Q point position can be determined through differential calculation of its linear interference spectrum. The Q point represents the point where the slope between the wave peaks and troughs is the greatest. While this approach provides a precise measurement, it introduces complexity and degrades the precision of intensity detection by the interferometer due to the inherent noise of the detector.

2.2 Principle of the ultrasonic detection technology based on the time-stretched swept laser

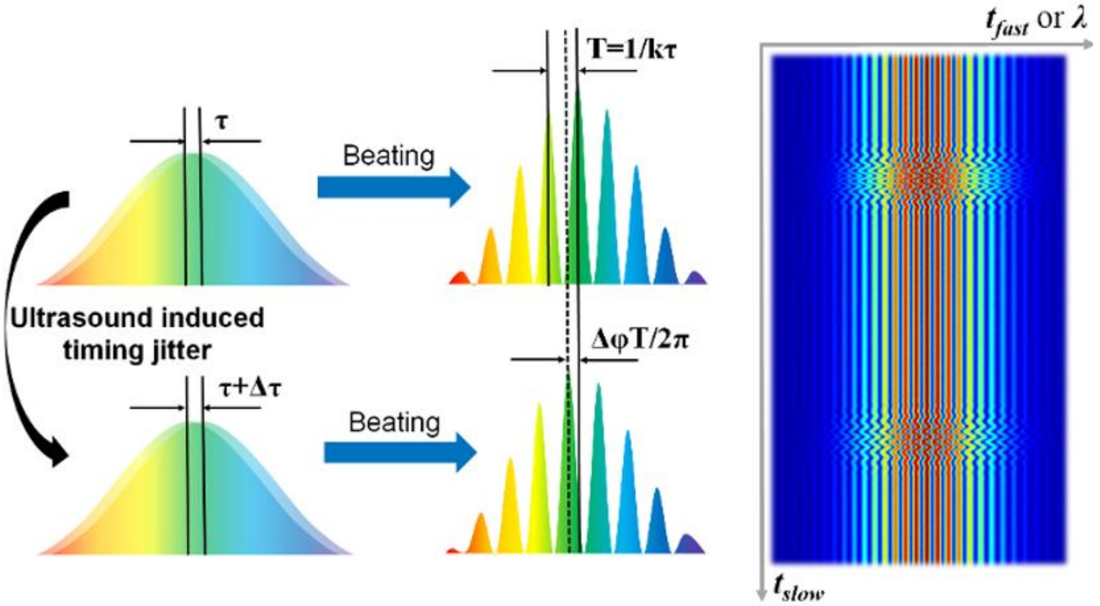

Fig. 3. Principle of the ultrasonic detection based on the time-stretched swept laser. The phase shifting of the interference pattern of the BFS is used to measure the timing jitter induced by the ultrasonic signal.

The ultrasonic pulses will induce the nanometer-level length change of the fiber, resulting in an attosecond-level timing jitter between the reference and signal lights. As shown in Fig. 3, when there is relative delay, τ_0, between reference and signal light, their BFS has an interference pattern with a period, T, of $1/k\tau_0$, where k is the linear frequency-sweeping slope of the light source. When the timing jitter, $\Delta\tau$, is induced by the ultrasonic signal, the relative delay is $\tau_0+\Delta\tau$. The interference pattern has an obvious phase shift, $\Delta\varphi$. The relationship between the timing jitter signal and phase shift of the BFS can be simply expressed by

$$\Delta\tau \approx \Delta\varphi/\omega_0, \tag{7}$$

where ω_0 is the center frequency of the swept source, which can be ensured by the OSA. Thus, the timing jitter signal can be measured by demodulating the phase shift of the BFS. Right part of Fig. 3 is the 2D evolution of the BFS and the corresponded ultrasonic signal. The time interval between two adjacent BFSs is the frequency-sweeping period of the swept source (sampling rate of t_{slow}). The movement of the interference pattern (phase shift, $\Delta\varphi$) can be used to orderly record the reference and echo ultrasonic pulses in order. Thus, the absolute distance between the PF detector and target can be measured by calculating the TOF between the reference and echo ultrasonic pulses, which will be subsequently further described. The detailed derivation of Eq. (1) and the calculation of $\Delta\varphi$ is included as followed.

The electrical field of the time-stretched swept laser can be expressed by:

$$A(t) = A_0(t)\exp\left\{ i\left[-2\pi\int^{t} f(\xi)d\xi - \omega_0 t \right] \right\}, \tag{8}$$

where A_0(t) is the amplitude of the swept laser, $f(\xi)$ is the instantaneous frequency, ω_0 is the carry freqeuncy of the swept source. To simplify the derivation process, we ignore the 3-order and higher-order dispersive effect of the dispersive medium. The electrical field of swept laser can be rewriten as:

$$A(t) = A_0(t)\exp\left[i\left(-\pi k t^2 - \omega_0 t\right)\right], \tag{9}$$

where k is the frequency sweeping slope. Thus, the BFS, $I(t)$, from the MZI with a relative delay, τ_0, can be expressed by:

$$\begin{aligned} i(t) &\propto \left|\sqrt{\kappa}\sqrt{\gamma}E(t) + \sqrt{1-\kappa}\sqrt{1-\gamma}E(t-\tau_0)\right|^2 \\ &= \kappa\gamma I_0(t) + (1-\kappa)(1-\gamma)I_0(t-\tau_0) + \\ &2\sqrt{\kappa\gamma}\sqrt{(1-\gamma)(1-\kappa)}A_0(t)A_0(t-\tau_0)\cos(2\pi k\tau_0 t - \pi k\tau_0^2 + \omega_0\tau_0) \end{aligned} \tag{10}$$

where $I_0(t)$ is the intensity of the time-domian profile, and κ and γ are the couple ratio of OC 1 and OC 2, respectively. The duration of $I_0(t)$ is usually nanosecond order, and τ_0 is picosecond order. When the pulse duration is far larger than τ_0, Eq. 10 can be further approached by:

$$i(t) \propto I_0(t)\begin{bmatrix} (1+2\kappa\gamma-\kappa-\gamma) + \\ 2\sqrt{\kappa\gamma}\sqrt{(1-\gamma)(1-\kappa)}\cos(2\pi k\tau_0 t - \pi k\tau_0^2 + \omega_0\tau_0) \end{bmatrix} \tag{11}$$

Here, we asume that $a=1+2\kappa\gamma-\kappa-\gamma$, $b=2\sqrt{\kappa\gamma}\sqrt{(1-\gamma)(1-\kappa)}$, $\omega_1=2\pi k\tau_0$, and $\varphi_1=-\pi k\tau_0^2+\omega_0\tau_0$. Eq. 11 can be simplified as:

$$i(t) \propto I_0(t)\left[a + b\cos\left(\omega_1 t + \varphi_1\right)\right] \tag{12}$$

The Fourier transform of $i(t)$ is

$$\psi(\omega) \propto aF_0(\omega) + b\frac{F_0(\omega-\omega_1)}{2}e^{i\varphi_1} + b\frac{F_0(\omega+\omega_1)}{2}e^{-i\varphi_1} \tag{13}$$

where $F_0(\omega)$ is the Fourier transform of $I_0(t)$. If the relative delay, τ_0, is properly set, the value of ω_1 can be far larger than the bandwidth of $F_0(\omega)$. In this case, we have

$F_0(-\omega_1) \approx 0$ and $F_0(-2\omega_2) \approx 0$. Then, $\omega = -\omega_1$ is substituted into Eq. 6, we have:

$$F\left(-\omega_1\right) \propto b\frac{F_0\left(0\right)}{2}e^{-i\varphi_1} \tag{14}$$

Thus, φ_1 can be obtained by:

$$\varphi_1 = -\angle\left[F\left(-\omega_1\right)\right] + \angle\left[F_0\left(0\right)\right]. \tag{15}$$

Obviously, we just care the change of φ_1, which carries the timing jitter information, $\Delta\tau$ (that is the variation of τ_0) caused by the ultrasonic signal. The second term is constant. Thus, the change of φ_1, $\Delta\varphi$, can be calculated by:

$$\Delta\varphi = \Delta\left\{-\angle\left[F\left(-\omega_1\right)\right]\right\}. \tag{16}$$

To obtain the relationship between $\Delta\tau$ and $\Delta\varphi$, we have:

$$\Delta\varphi = \varphi_1\left(\tau_0 + \Delta\tau\right) - \varphi_1\left(\tau_0\right) = \left(-\omega_1 - \frac{\omega_1\Delta\tau}{2\tau_0} + \omega_0\right)\Delta\tau. \tag{17}$$

Because $\omega_1/2\pi$ is the freqeuncy of the inteference pattern of the BFS, which obviously has to be less than the practicle detection bandwidth of 16 GHz. Therefore, compared with the third term, the first and second terms can be ignored. Thus, the timing jitter induced by the ultrasonic signal can be linearly mapped by the phase change. Then, we have:

$$\Delta\tau \approx \Delta\varphi/\omega_0, \tag{18}$$

2.3 Experimental setup

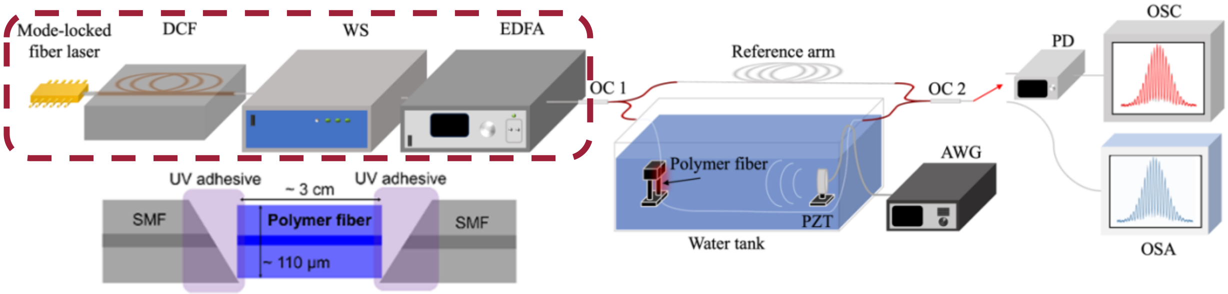

Fig. 4. Experimental setup of the proposed underwater ultrasonic ranging system.

The experimental setup of the underwater ultrasonic ranging system is shown in Fig. 4. The time-stretched swept laser is shown inside the red dashed box. The commercial mode-locked fiber laser (C-Fiber Menlo System) with a repetition rate of 100.1 MHz is injected into a piece of dispersion compensation fiber (DCF) with a total dispersive coefficient of 162 ps/nm for time stretching. Then, the huge chirped pulse is spectrally filtered by a wave shaper (WS, 4000s, Finisar) to avoid the time-domain overlapping between two adjacent time-stretched pulses. The filtered swept light is amplified by an erbium-doped fiber amplifier (EDFA) to generate the final output of the swept source. In the underwater ranging system, we use the coherent detection method to measure the ultrasonic signal. Thus, the time-stretched swept laser is injected into the MZI consisted by the reference arm, signal arm and 2 optical couplers (OC 1 and OC 2) with the coupling ratio of 5:5. A variable delay line (VDL) in the reference arm is used to adjust the optical path deference of the MZI to ensure the effective overlap between the reference and signal lights. Then, the BFS generated from the MZI is detected by a photodetector (PD, 2150R, Finisar) and the oscilloscope (OSC, DSA-X, 96204Q, Agilent).

To further increase the sensitivity, we used a homemade polymer fiber (PF) with a small Young's modulus as the ultrasonic detector. This PF, with a length of 3 cm, a cladding diameter of 110 μm, and a core diameter of 7 μm, was employed for this purpose. The PF is inserted into the signal arm, which is submerged in the water tank. As shown as the bottom left of Fig. 1, the PF is connected with two pieces of the single-mode fiber (SMF) by the UV adhesive. To avoid the reflected light from two end faces of the SMF to generate the unwanted FP interference effect, the SMF is cut with an angle of about 60 degrees. Compared with the SiO_2 fiber, the PF with a lower Young modulus has a much higher detection sensitivity.

In contrast, constructing a high-speed underwater communication system utilizing ultrasound transducers necessitates selecting the highest frequency possible, as the bandwidth limitation of the transducer restricts the achievable frequency range. Higher frequencies correspond to larger bandwidths. Consequently, this limitation necessitates frequency response measurements. In this scenario, we opted for an ultrasonic transducer operating at 11 MHz, which possesses a bandwidth of 2.2 MHz.

2.4 Expermintal results

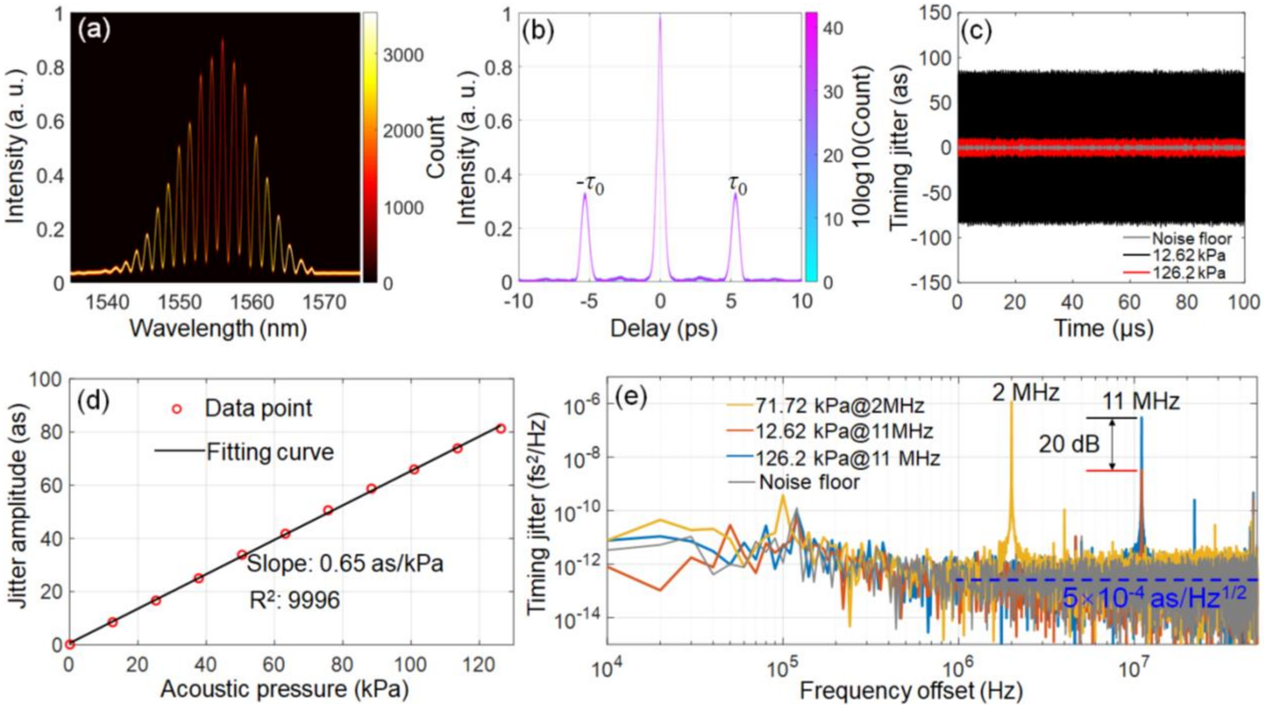

Fig. 5. (a) 2D statistical histogram of the BFS from the MZI; (b) amplitude of the FFT of the BFS; (c) detected sinusoidal ultrasonic signals with the acoustical pressures of 12.6 kPa and 126.2 kPa and the noise floor; (d) jitter amplitudes under 11 MHz ultrasonic signal with the acoustic pressure changed from 0 to 126.2 kPa; (e) PSD curves of the sinusoidal ultrasonic signals under the acoustical pressures of 12.6 kPa and 126.2 kPa with the frequency of 11 MHz and 71.7 kPa with the frequency of 2 MHz and the corresponded noise floor.

Firstly, we study the detection results of the simple sinusoidal ultrasonic signal, and demonstrate its linear response property of the ultrasonic detection system. To study the noise floor of the system, the arbitrary waveform generator (AWG, Precision BK, 4065) is firstly turned off. Thus, the BFSs with a repetition rate of 100.1 MHz from the MZI is continuously acquired by the OSC. The eye diagram obtained by calculating the statistical histogram of 40045 shots of BFSs within 0.4 ms from the MZI is shown in Fig. 5. (a). The shape of the interference pattern is very clear, indicating the position of the pattern almost unchanged without the ultrasound wave. The corresponded eye diagram of the amplitude-frequency curve of the BFSs is shown in Fig. 5. (b), where two components are located at $-\tau_0$, 0 and τ_0 (τ_0=5.3 ps), respectively. Thus, the noise floor curve in the time domain can be calculated by the phase value of the Fourier transform of the BFS at $\tau=\tau_0$, which is shown as the gray curve in Fig. 5. (c). The standard deviation (std.) of the noise floor is about 1.2 as, demonstrating that the system owns the ability to response the attosecond-level timing jitter induced by the weak ultrasonic signal. Then, the AWG is turned on, and the sinusoidal ultrasonic signal with a frequency of 11 MHz is stimulated by the UT. The ultrasonic signal cases a sinusoidal length change of the PF. The detected timing jitter signals under the acoustical pressure of 12.6 kPa and 126.2 kPa are shown as the black and red curves, respectively. The jitter amplitudes are 8.46 as and 81.39 as, respectively.

To confirm its linear response property, we adjust the acoustical pressure from 0 kPa to 126.2 kPa with a step of 12.6 kPa, and the corresponded jitter amplitude are shown in Fig. 5. (d). The jitter amplitude has a linear relationship with the acoustical pressure, and the linear fitting R^2 reaches 0.9996. The detection slope is 0.64 as/kPa. To confirm the ultrasonic frequency, we plot the power spectral densities (PSDs) of the timing jitter curves under the acoustical pressures of 12.6 kPa (red curve) and 126.2 kPa (blue curve) with the frequency of 11 MHz and 71.7 kPa (yellow curve) with the frequency of 2 MHz. There are three signal peaks located at 11 MHz and 2 MHz, respectively. At the frequency offset of 11 MHz, the signal peak intensity is exactly decreased by ～20 dB, when the acoustical pressure is changed from 126.2 kPa to 12.6 kPa. To estimate the detection limit, the PSD of the noise floor curve (gray curve) is plot in Fig. 5. (e), where the noise distribution is flattened in the frequency from 1 MHz to 50 MHz. As shown as the blue dashed curve, the average value of the noise floor within this frequency offset region is about 6.9×10^{-4} as/Hz$^{1/2}$, corresponding to the noise equivalent pressures (NEP) of 0.53 Pa/Hz$^{-1/2}$@11MHz and 0.16 Pa/Hz$^{-1/2}$@2MHz. These experimental results indicate the linear response property and ability for the detection of high-frequency ultrasound wave.

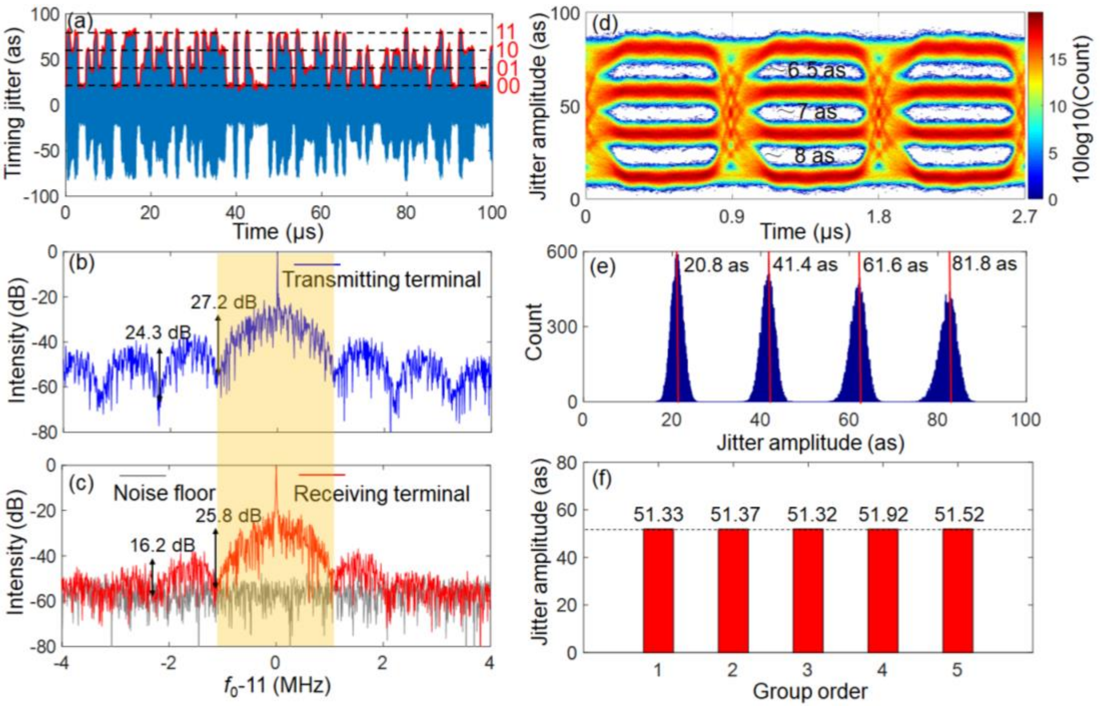

Fig. 6. (a) Detected timing jitter signal with the PAM-4 modulation; frequency spectra of the electrical driving signal in the transmitting terminal (b) and the measured timing jitter signal in the receiving terminal (c); (d) eye diagram of

the PAM-4 codes demodulated from the timing jitter signal; (e) statistical histogram of the jitter amplitudes of the PAM-4 codes; (f) average values of the jitter amplitudes of the PAM-4 codes in different data groups.

To experimentally demonstrate its ability to transmit PAM-4 signal, we add the amplitude modulation with the PAM-4 format on the sinusoidal ultrasonic signal with a frequency of 11 MHz due to the narrow bandwidth limitation of the UT. The distance between the detector and the UT 1 is about 0.1 m. The detected timing jitter signal is shown as the blue curve in Fig. 6. (a), and the red curve is the envelope of the timing jitter signal. To demonstrate the accuracy of this system, we program a pseudo random bit sequence signal mapped with PAM-4 modulation. The amplitude is randomly coded within 4 kinds of levels (00, 01, 10, 11). We use 5 groups of the data; every group has 11000 codes. Due to the bandwidth limitation from the ultrasound transducer, the highest amplitude switch rate is 1.1 MHz, corresponding to a data rate of 2.2 Mbps. The frequency spectra of the driving electrical signal in the transmitting terminal and the detected ultrasonic signal in receiving terminal are shown in Fig. 6. (b) and 6. (c). UT 1 has a bandwidth of about 2 MHz. In the frequency range from –1.1 MHz to 1.1 MHz (marked by the yellow highlighted part), the spectra in the transmitting and receiving terminal are coincided with each other well, and the contrasts of the main lobes are 27.2 dB and 25.8 dB. Due to the noise floor, the contrasts of 2 order sidelobes are 24.3 dB and 16.2 dB. The intensity of the 2 order sidelobe in the transmitting terminal are obviously attenuated, resulted from the bandwidth limit of the UT. To evaluate the quality of the received signal, we plot the corresponded eye-diagram, as shown as Fig. 6. (d). To demonstrate the stability of the detection system with the MZI free running, the time interval of the acquisition of adjacent two groups is 10 min. The eye diagram has 4 amplitude levels with the eye heights of 6.5 as, 7 as and 8 as, indicating the good isolation of each level. The statistical histogram of the amplitudes of all 55000 codes are shown in Fig. 6. (e). These codes are distributed in 4 different regions with the peaks located at 20.8 as, 41.4 as, 61.6 as and 81.8 as, respectively. There is no inter-symbol interference, indicating the successful detection of the random ultrasonic signal and its potential application in the underwater communication. The averaged jitter amplitude of the 11000 PAM-4 symbol in every group is shown as Fig. 6. (f), where the amplitude value slight varies from 51.31 as to 51.92 as, indicating the excellent long-term stability of the detection sensitivity with the whole system free running. Different from the traditional ultrasonic detection based on the single-frequency laser, the proposed setup need not any servo feedback devices to stabilize the phase of the MZI.

2.5 Summary

In this work, the concept of TSSCD is introduced and demonstrated with a TSSCD-based UWAC system corresponding to the NEP of 0.53 Pa/Hz$^{-1/2}$, supporting data rates up to 2.2 Mbps. This system applied the amplitude modulation with the PAM-4 format on the sinusoidal ultrasonic signal with a frequency of 11 MHz, receiving the ultrasound signal by a TP fiber, and recovering the transmission signal by calculating the timing jitter between two arms of the MZI.

Chapter 3

Experimental Demonstration of 520-Mbps LED-based UWOC Utilizing Nonlinear Weighted DFE

Chapter 3 introduces the fundamental principles and computational complexity of post-equalizer. Subsequently, the principle of NWDFE is presented and experimentally validated. The system utilized the Reliability block and Use block as substitutes for the hard-decision feedback symbol in VFFE-DFE, thereby adopting a soft-decision approach grounded in a compressed sigmoid nonlinear function. This alteration significantly diminished the likelihood of error propagation and bolstered the equalization performance.

3.1 Principle and computational complexity of the post-equalizer

I. FFE, P-NFFE

The Finite Impulse Response (FFE) is a widely used and reliable linear equalizer designed to tickle the effects of linear inter symbol interference (ISI). At n_{T}^{th} symbol, the equalized output $y_{\mathrm{FFE}}(n_{\mathrm{T}})$ of FFE operating at two samples per symbol (T/2 spaced) is expressed as:

$$y_{FFE}(n_T) = \sum_{k=-\frac{N_1}{2}}^{\frac{N_1}{2}-1} h_1(k)x(n_{T/2} - k), \tag{19}$$

where $n_{\mathrm{T}/2} = \frac{n_{\mathrm{T}}}{2}$ is the index of sample duration; $x(n-k)$ is the linear input term; $h_1(k)$ is the linear weight of N_1-tap FFE equalizer. For convenience, *n* represents n_{T} and $n_{\mathrm{T}/2}$ in the following contents.

Additionally, the nonlinearities arising from electrical amplifiers, modulators, and PD should be taken into account. Consequently, nonlinear FFEs are frequently employed to compensate for these nonlinearities, such as the second-order P-NFFE. P-NFFE involves the addition of the second-order terms of the input and the N2 -tap filter, resulting in equalized outputs from the supplementary convolutions.

$$y_{\mathrm{P-NFE}}(n) = \underbrace{\sum_{k=-\frac{N_1}{2}}^{\frac{N_1}{2}-1} h_1(k)x(n-k)}_{\mathrm{FFE}} + \underbrace{\sum_{k=-\frac{N_2}{2}}^{\frac{N_2}{2}-1} h_2(k)x^2(n-k)}_{2^{nd}\mathrm{Pterms}}, \tag{20}$$

where $x^2(n-k)$ and $|x(n-k)|$ are the 2nd-order nonlinear term and the absolute term, respectively; $h_2(k)$ is the corresponding weights.

P-NFFE is a simplified variant of Volterra series-based nonlinear FFE (V-NFFE). It considers only self-beating terms in the nonlinear terms and ignores cross-beating terms for simplicity, though this may degrade performance.

$$y_{\mathrm{V-NFFE}}(n) = \sum_{k=-\frac{N_1}{2}}^{\frac{N_1}{2}-1} h_1(k)x(n-k) + \sum_{l=0}^{N_2-1} \sum_{k=-\frac{N_2}{2}}^{\frac{N_2}{2}-1-l} h_2(k,l)x(n-k)x(n-k-l) \tag{21}$$

Obviously, the RNRMs of FFE and P-NFFE are N_1 and N_1+2N_2, respectively. Note that the RNRM of the second-order V-NFFE is $N_1 + N_2^2 + N_2$.

II. FFE-DFE

To effectively address spectral notches through pole insertion, a decision-feedback equalizer (DFE) with an infinite impulse response (IIR) structure emerges as a promising solution. However, such a DFE is susceptible to error propagation stemming from decision blocks. Consequently, integrating a robust feedforward equalizer (FFE) with a DFE, referred to as FFE-DFE, or pairing a robust nonlinear feedforward equalizer (NFFE) with a DFE, known as NFFE-DFE, represents the optimal strategy for equalization. In these configurations, the DFE's IIR structure adeptly equalizes spectral notches via pole insertion. It is crucial to highlight that the DFE functions at a rate of one sample per symbol (T spaced). The equalized outputs of the FFE-DFE can subsequently be articulated as follows:

$$y_{\text{FFE-DFE}}(n) = \underbrace{\sum_{k=-\frac{N_1}{2}}^{\frac{N_1}{2}-1} h_1(k)x(n-k)}_{\text{FFE}} + \underbrace{\sum_{k=1}^{D_1} l_1(k)d(n-k)}_{\text{DFE}}, \qquad (22)$$

where $d(n-k)$ and l_1 are the decision term of the last equalized output $y(n_{\text{T}}-k)$ and the corresponding weight of the D_1 -tap filter, respectively.

3.2 Principle of proposed NWDFE

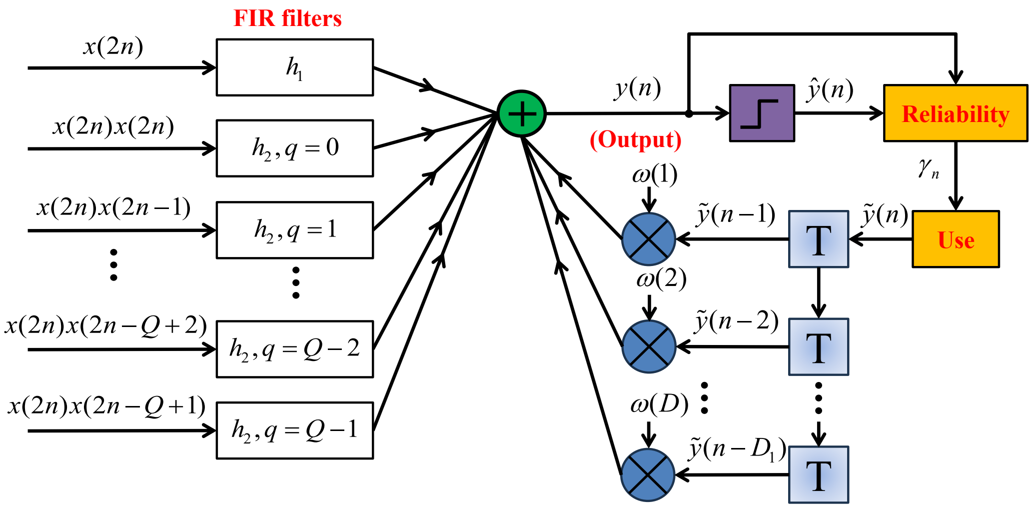

Fig. 7. Schematic diagram of the NWDFE.

To mitigate the linear ISI and nonlinear distortion while maintaining similar complexity as VFFE-DFE, a NWDFE consisting of a 2nd-order diagonally-pruned

VFFE and a WDFE is introduced for LED-based UWOC system. The VFFE is used to equalize the nonlinear distortion while the WDFE can address the ISI caused by bandwidth limitation and reduce the error propagation probability. Fig. 7 illustrates the schematic diagram of the NWDFE. The inclusion of a reliability block and a use block in the NWDFE, followed by symbol decision, distinguishes it from the VFFE-DFE.

The *n*th sample of the output of NWDFE can be expressed as:

$$\begin{aligned} y(n) = & \sum_{k=0}^{N_1-1} h_1(k)x(2n-k) + \sum_{k=1}^{D} \omega(k)\tilde{y}(n-k) \\ & + \sum_{q=0}^{Q-1} \sum_{k=0}^{N_2-1-q} h_2(k,q)x(2n-k)x(2n-k-q) \end{aligned} \tag{23}$$

where $x(n)$ with $T/2$ symbol space and $y(n)$ are the sequences before and after the equalization, respectively. N_K and h_K are the memory length of the VFFE and K^{th}-order ($K = 1, 2$) kernel, respectively. Value Q denotes as the pruning factor used to prune the unimportant cross-beating terms. D and ω are the memory length of DFE and kernel, respectively. The 2nd-order nonlinear WDFE term is omitted here for simplicity since it has a negligible impact on the equalization performance. The soft-decision feedback symbol $\tilde{y}(n)$ is a combination of the previous equalizer output

$y(n)$ and the previous hard-decision output $\hat{y}(n)$, which is given by [71]:

$$\begin{aligned}\tilde{y}(n) &= f(\gamma_n)\hat{y}(n) + \left[1 - f(\gamma_n)\right] y(n) \\ &= y(n) + f(\gamma_n)\left[\hat{y}(n) - y(n)\right]\end{aligned} \tag{24}$$

where γ_n and $f(\gamma_n)$ are the reliability value and the compressed sigmoid nonlinear function, respectively, which can be calculated by [70], [71]:

$$\gamma_n = \begin{cases} 1 - \left|y(n) - \hat{y}(n)\right|, \text{if} \left|y(n)\right| < M - 1 \\ \qquad 1, \qquad \text{else} \end{cases} \tag{25}$$

$$f(\gamma_n) = \frac{1}{2}\left(\frac{1 - \exp\left[-a(\frac{\gamma_n}{b} - 1)\right]}{1 + \exp\left[-a(\frac{\gamma_n}{b} - 1)\right]} + 1 \right) \tag{26}$$

where *M* represents the level of the PAM symbols, *a* is a positive integer that defines the steepness of the function $f(\gamma_n)$, and *b* with $0 < b \leq 1$ is a compression factor. According to Eqs. (23)-(26), the NWDFE requires only one additional real-valued multiplication compared to VFFE-DFE.

3.3 Experimental setup and Results

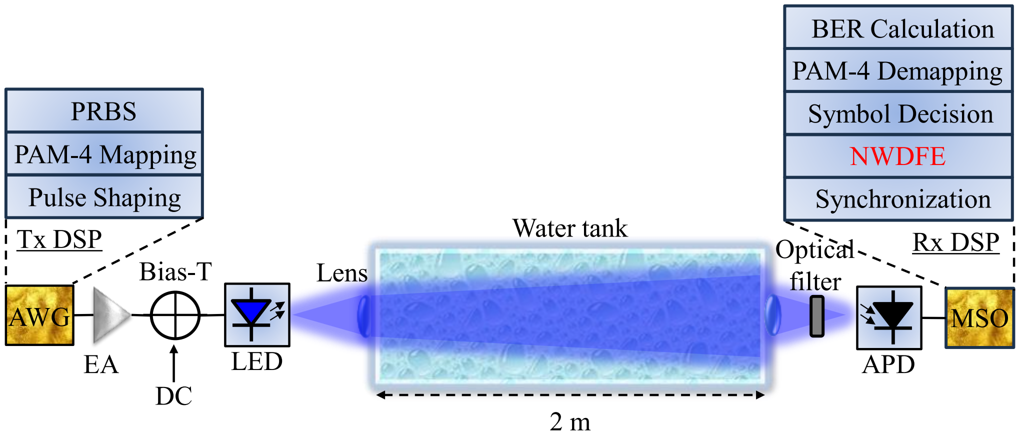

Fig. 8. Experimental setup and the employed DSP of blue-LED-based UWOC system.

The performance evaluation of the NWDFE was conducted within a blue-LED-based UWOC system, utilizing the experimental setup and DSP depicted in Figure 8. At the transmitter end, PAM-4 symbols were initially mapped with a pseudo-random bit sequence (PRBS). Following this, the PAM-4 symbols underwent up-sampling to achieve 2 samples per symbol, which facilitated pulse shaping via a 0.1-roll-off raised cosine (RC) filter. Post resampling, the resultant PAM-4 signal was loaded into an arbitrary waveform generator (AWG, Keysight 8199A) that operated at a sample rate of 1 GSa/s, enabling digital-to-analog (D/A) conversion. The analog signal output was subsequently amplified by an electrical amplifier (EA, ZHL-2-8-S+), and then attenuated by 2 dB electrically. After coupling with a direct current (DC) bias through a bias-T, the combined signals were introduced into a 450-nm

LED. The emitted blue light was focused through a lens before entering an acrylic water tank, which had dimensions of 2 m in length, 0.4 m in width, and 0.4 m in height. After traversing a 2-m aquatic channel, the output beam from the water tank was passed through a lens and directed into an APD (Hamamatsu C5658). Ultimately, the detected PAM-4 signal was captured and stored by a mixed signal oscilloscope (MSO, Keysight MSOS404A) operating at a sample rate of 1 GSa/s, for subsequent off-line DSP. The DSP procedures included resampling to 2 samples per symbol, synchronization, equalization using the NWDFE, symbol decision, PAM-4 demapping, and BER calculation. During the training phase, a total of 10000 symbols were transmitted to estimate kernel coefficients using the recursive least-squares (RLS) algorithm, which remained constant throughout the equalization process.

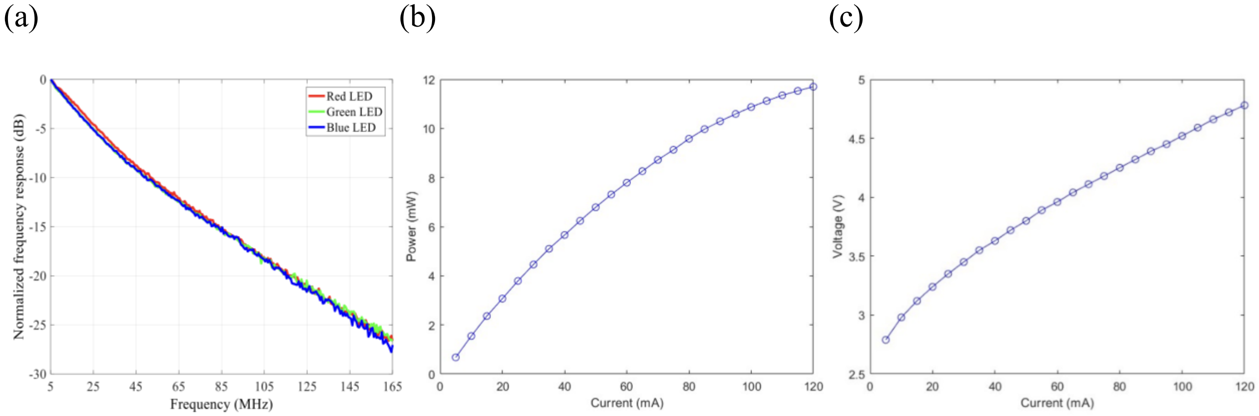

Fig. 9. (a) The Frequency response of the CREE RGB LED; (b) The I-V curve of the blue LED; (c) The I-P curve of the blue LED.

The performance of the proposed PAM-4 Blue LED-based UWOC system is experimentally investigated in indoor environment. Fig. 9. (a) shows the frequency response curve of the *CREE* RGB LED. The power-current-voltage characteristic of the used 450-nm Blue LED is measured, as shown in Fig.9. (a) and (b). The range for linear working current of the LED is 90 to 95 mA. The BER performance behaves the best at 95mA.

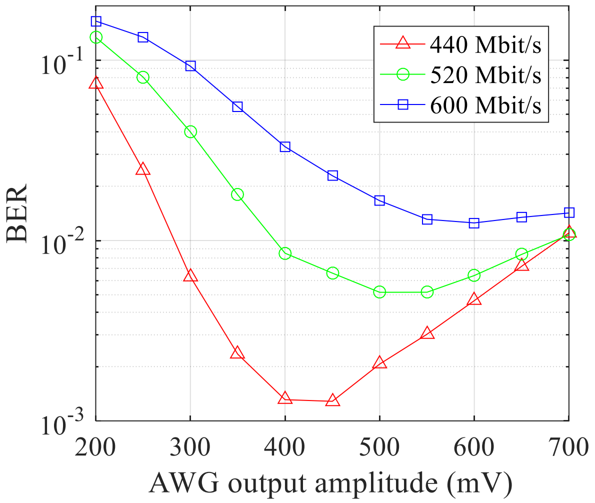

Fig. 10. BER versus the AWG output amplitude using VFFE-DFE under different data rates.

Prior to optimizing the memory lengths, pruning factor, and parameters a and b of the compressed sigmoid nonlinear function, we first optimize the RF power based on the output amplitude of the AWG using VFFE-DFE under different data rates. Three Baud rates of 220 MBaud, 260 MBaud, and 300 MBaud are employed for PAM-4 signals while maintaining a received optical power (ROP) of -9.35 dBm. To get convergent performance, memory lengths and pruning factor of the VFFE-DFE are chosen as $N_1 = 24$, $D_1 = 16$, $N_2 = 24$, and $Q = 6$. The BER performance of VFFE-

DFE is improved before reaching the optimal level. This can be attributed to the fact that when the AWG output amplitude is low, increasing the RF power can improve the SNR. From Fig. 10, we can observe that when the AWG output amplitude is further increased, the nonlinear distortion becomes stronger, thereby deteriorating the BER performance. Moreover, employing a higher Baud rate or signal bandwidth necessitates an increased RF power due to severer bandwidth limitations of the components in UWOC system. Based on the BER results, the optimal AWG output amplitudes for 440 Mbps, 520 Mbps and 600 Mbps PAM-4 UOWC transmissions are determined as 450 mV, 500 mV, and 600 mV, respectively.

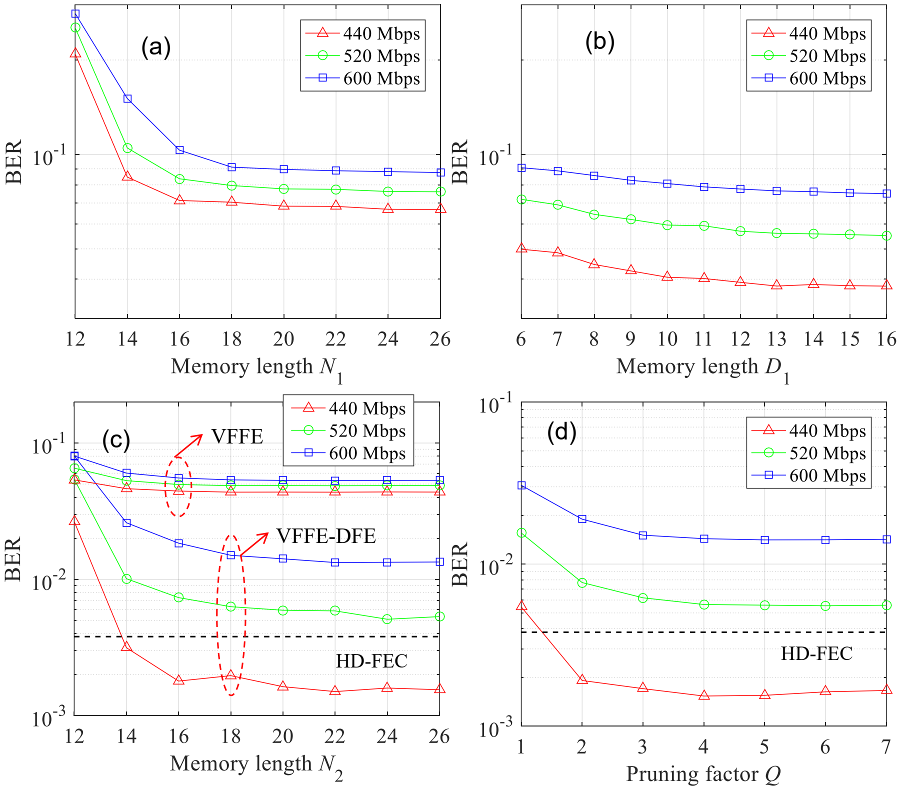

Fig. 11. (a) BER versus linear memory length N1 for FFE; (b) BER versus linear memory length D for FFE-DFE with N1 = 20; (c) BER versus nonlinear memory length N2 for VFFE and VFFE-DFE; (d) BER versus pruning factor Q

for diagonally-pruned VFFE-DFE.

We then optimize the linear and nonlinear memory lengths of VFFE-DFE though the blue-LED-based UWOC system at a ROP of -9.35 dBm. Fig. 11. (a) shows the BER versus the linear memory length N_1 for FFE under different data rates. The BERs of all cases decrease as the memory lengths increase and then reach saturation at $N_1 = 20$. The BER as a function of the linear memory length D for FFE-DFE at $N_1 = 20$ is presented in Fig. 11. (b). The optimal BERs for FFE-DFE under different data rates are achieved at $D = 14$. By fixing $N_1 = 20$ and $D = 14$, the BER versus the nonlinear memory lengths N_2 for the VFFE-DFE and VFFE without diagonal pruning are demonstrated in Fig. 11. (c). It demonstrated that the VFFE-DFE can achieve superior performance compared to the VFFE in compensating for both linear ISI and nonlinear distortion under a bandwidth limited UWOC channel. Despite the BERs of VFFE and DFE failing to meet the 7% HD-FEC BER limit of 3.8×10^{-3}, the VFFE-DFE achieves successful UWOC transmission at a data rate of 440-Mbps when $N_2 \geq 14$. In order to balance the performance and complexity, $N_2 = 20$ is applied. Similarly, Fig. 11. (d) shown that the optimal BERs are achieved when the pruning factor U of VFFE-DFE is selected as $Q = 4$.

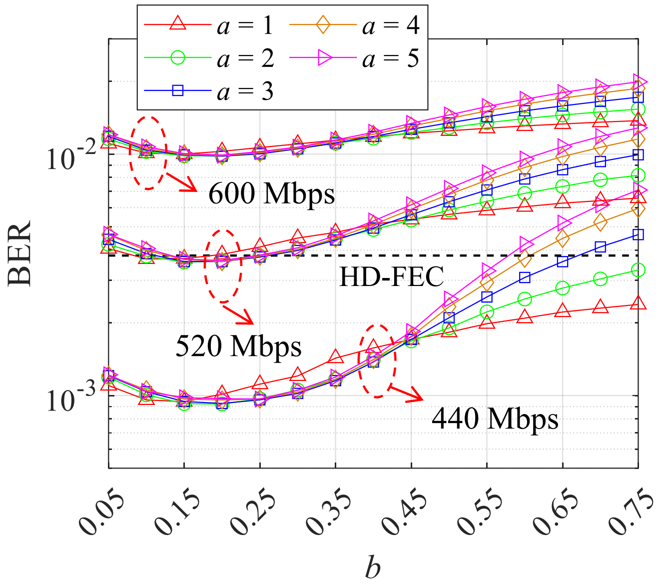

Fig. 12. BER as a function of compression factor b for NWDFE.

The performance of NWDFE is evaluated by replacing the hard decision output in VFFE-DFE with the soft decision one, based on the optimized parameters $N_1 = 20$, $N_2 = 20$, $Q = 4$, $D_1 = 14$. The measured BER versus the compression factor b at different values of parameter a using NWDFE is depicted in Fig. 12. It can be observed that $a = 2$ and $b = 0.15$ are suitable for the 520-Mbps case, while $a = 2$ and $b = 0.2$ should be applied to 440-Mbps and 600-Mbps cases, respectively. Furthermore, owing to the reduced probability of the error propagation [70], [71], the blue-LED-based UWOC system using NWDFE achieves successful transmission at a rate of 520 Mbps.

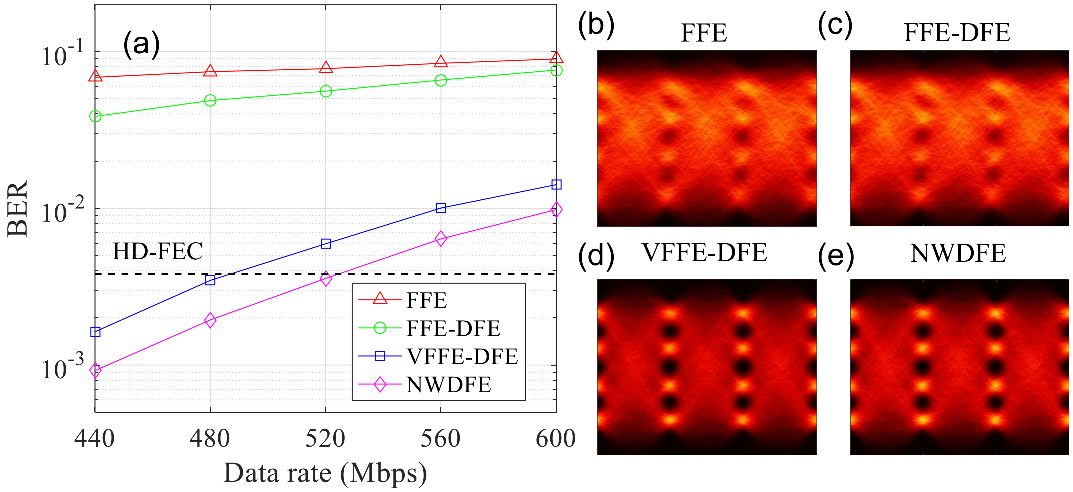

Fig. 13. (a) BER versus data rate using different equalizers after 2-m aquatic transmission at a ROP of -9.35 dBm; (b)-(e) recovered eye diagrams of 480-Mbps PAM-4 signals using different equalizers.

Finally, we compare the performance of NWDFE with other conventional equalizers based on the 2-m blue-LED-based UWOC system. Fig. 13. (a) shows the BER versus the data rate using different equalizers at a ROP of -9.35 dBm. The BERs of FFE and FFE-DFE fail to reach the 7% HD-FEC limit of 3.8×10^{-3} at a data rate of ≥ 440-Mbps. The switch from VFFE-DFE to NWDFE enables an increase in data rate from 480 Mbps to 520 Mbps, resulting in a capacity improvement of approximately 9%. Meanwhile, the complexities of both NWDFE and VFFE-DFE remain similar. The received eye diagrams of 480-Mbps PAM-4 signals using FFE, FFE-DFE, VFFE-DFE and NWDFE are shown in Fig. 13. (b)-13. (e), respectively. Notably, the eye diagram of NWDFE is more distinguishable than those of other three equalizers.

3.4 Summary

In this work, we have experimentally demonstrated a 520-Mbps PAM-4 blue-LED-based UWOC system employing a NWDFE to equalize the linear ISI and nonlinear distortion. Experimental results show that the NWDFE with soft-decision has achieved an approximately 9% increase in data rate compared to the VFFE-DFE, while maintaining similar equalization complexity.

Chapter 4

Conclusion and future work

4.1 Conclusion

The increasing demand for oceanographic research, underwater resource exploration, and tactical surveillance has highlighted the limitations of conventional underwater radio frequency (UWRF) communication systems compared to underwater acoustic communication (UWAC) and underwater optical communication (UWOC) systems, particularly in terms of transmission distance and speed.

For long-range transmission, UWAC systems often use MIMO technology to enhance performance. However, massive MIMO systems require compact, highly sensitive detector arrays and centralized processing units. Traditional passive sonar-based systems are not ideal for MIMO due to the bulkiness of hydrophones and the high cost and inconvenience of connecting them to a central processing unit. Fiber-optic ultrasonic sensors have gained attention for their immunity to electromagnetic interference and compact size. Conventional fiber sensing probes, typically based on Bragg gratings, short-cavity fiber lasers, or interferometers, have limitations such as poor frequency response and complex fabrication processes. Interferometer-based sensors are preferred for their wide frequency bandwidth and ease of fabrication, but they require a tunable narrow linewidth laser phase-locked for high sensitivity and stability, complicating the setup. Additionally, the precision of intensity detection is affected by detector noise. Recently, the time-stretched self-coherent detection (TSSCD) system has been used to measure attosecond-level timing jitter between pulses, inspiring its application in UWAC systems to enhance sensitivity. The ultrasonic signal from the transducer causes nanometer-level length changes in the PF-based ultrasonic detector, inducing attosecond-level timing jitter in the signal light. This jitter can be precisely recorded by the phase change of the Brillouin frequency shift (BFS) of the swept source generated from the Mach-Zehnder interferometer (MZI). The ultrafast sweeping rate of the light source allows for a maximum measurement bandwidth of 50 MHz, enabling the detection of wideband ultrasonic signals.

In this study, we demonstrated a novel 2.2-Mbps PAM-4 UWAC system based on TSSCD with PF to receive the ultrasound signal, achieving noise equivalent pressures (NEP) of 0.53 Pa/Hz^1/2 at 11 MHz and 0.16 Pa/Hz^1/2 at 2 MHz. These results indicate that this UWAC system has high sensitivity, a linear response, and the capability to detect high-frequency ultrasound waves, thereby improving bandwidth for future long-range transmission development.

For mid-range transmission, LED-based underwater optical communication (UWOC) systems are ideal for scenarios requiring a large field of view (FOV), relaxed alignment, and auxiliary lighting due to their wide divergence angle and compatibility with natural illumination. However, these systems face bandwidth limitations and nonlinear distortion, which degrade transmission performance. Nonlinear distortion primarily arises from the modulation nonlinearity of LEDs, as well as from electrical amplifiers and photoreceivers (PDs), with LED modulation nonlinearity being the most significant factor. To address this issue, 2nd-order and 3rd-order Volterra feedforward equalizers (VFFE) are commonly used to compensate for nonlinear distortion in LED-based UWOC systems. These equalizers can accurately model the complex time-dispersive nonlinear channel response. Additionally, integrating VFFE with a decision feedback equalizer (DFE), known as VDFE, can significantly enhance transmission performance in bandwidth-limited LED-based UWOC systems compared to using VFFE alone. However, VDFE is prone to error propagation if incorrect symbol decisions are made. To mitigate error propagation, the decision feedback equalizer can be relocated to the transmitter side, a technique known as Tomlinson-Harashima precoding (THP). While THP effectively prevents error propagation, it suffers from pre-coding loss and requires precise channel feedback.

In this study, we experimentally demonstrated a 520-Mbps PAM-4 blue-LED-based UWOC system employing a NWDFE by combining 2nd-order VFFE and weighted DFE to equalize linear inter-symbol interference (ISI) and nonlinear distortion. The core concept of NWDFE involves substituting the hard-decision feedback symbol used in VFFE-DFE with a soft-decision symbol derived from a compressed sigmoid nonlinear function. This approach significantly lowers the probability of error propagation and improves the overall equalization performance. The experimental results show that the NWDFE with soft-decision achieved approximately a 9% increase in data rate compared to the VFFE-DFE, while maintaining similar equalization complexity.

4.2 Prospect

Although preliminary research results have been obtained, certain issues and protocols necessitate further investigation due to experimental limitations and time constraints. Building on the current work, we suggest several potential directions for future research.

Our proposed TSSCD based UWAC system can be applied with MIMO technology to achieve higher data rate and efficiency. The proposed TSSCD system in **Chapter 2** focuses primarily on single channel. To achieve MIMO system, the multi-channel

TSSCD system can independently carry the phase that precisely maps with the timing jitter information in different channels. Based on the equations in **Chapter 2**, the detected light intensity of the BFS outputted from the 2-channel TSSCD can be expressed by:

$$\begin{aligned} I(t) &= A_0^2(t) + \sum_{m=1,2} A_0^2(t-\tau_m) + 2\sum_{m=1,2} A_0(t) A_0(t-\tau_m)\cos\left(2\pi k\tau_m t - \pi k {\tau_m}^2 + \omega_0\tau_m\right) \\ &+2A_0(t-\tau_1)A_0(t-\tau_2)\cos\left[2\pi k(\tau_2-\tau_1)t - \pi k\left({\tau_2}^2-{\tau_1}^2\right)+\omega_0(\tau_2-\tau_1)\right]. \end{aligned} \tag{17}$$

Considering the duration of the chirped pulse is usually nanosecond order, with the slow envelope approximation, Eq. (17) can be further simplified with Fourier transform of $I(t)$ as:

$$\begin{aligned} F(\omega) &\propto 3F_0(\omega) + F_0(\omega-\omega_1)\exp(i\varphi_1) + F_0(\omega+\omega_1)\exp(-i\varphi_1) + F_0(\omega-\omega_2)\exp(i\varphi_2) \\ &+F_0(\omega+\omega_2)\exp(-i\varphi_2) + F_0(\omega-\omega_d)\exp(i\varphi_d) + F_0(\omega+\omega_d)\exp(-i\varphi_d), \end{aligned} \tag{18}$$

where $F_0(\omega)$ is the Fourier transform of $I_0(t)$. We can obtain multiple frequency components in the Fourier domain, which are located at $\omega=0$, $\omega=\pm\omega_1$, $\omega=\pm\omega_2$ and $\omega=\pm\omega_d$. Thus, substitution of $\omega=-\omega_1$ into Eq. (20), respectively, we have:

$$\begin{aligned} F(-\omega_1) &\propto 3F_0(-\omega_1) + F_0(-2\omega_1)\exp(i\varphi_1) + F_0(0)\exp(-i\varphi_1) + F_0(-\omega_1-\omega_2)\exp(i\varphi_2) \\ &+F_0(\omega_d)\exp(-i\varphi_2) + F_0(-\omega_2)\exp(i\varphi_d) + F_0(-\omega_1+\omega_d)\exp(-i\varphi_d). \end{aligned} \tag{19}$$

By the proper adjustment of τ_1 and τ_2 and inducing enough dispersive, we can make the bandwidth of $F_0(\omega)$ less than ω_1, ω_2, $\omega_1+\omega_2$, ω_d and $-\omega_1+\omega_d$. The first, second, fourth, fifth, sixth and seventh term can be totally ignored. φ_1 and φ_2 can be calculated by:

$$\varphi_1 = -\square\left[F\left(-\omega_1\right)\right] + \square\left[F_0\left(0\right)\right]. \tag{20}$$

$$\varphi_2 = -\square\left[F\left(-\omega_2\right)\right] + \square\left[F_0\left(0\right)\right]. \tag{21}$$

Next, we determine the relationship between phase change and timing jitter ($\Delta\tau_1$ and $\Delta\tau_2$) induced by the ultrasound signal. When the timing jitter $\Delta\tau_1$ and $\Delta\tau_2$ is weak ($\Delta\tau_1 \ll \tau_1$ and $\Delta\tau_2 \ll \tau_2$), the induced phase change in channel 1 and channel 2 can be written as

$$\Delta\varphi_1 = \varphi_1\left(\tau_1 + \Delta\tau_1\right) - \varphi_1\left(\tau_1\right) = \left(-\omega_1 - \frac{\omega_1\Delta\tau_1}{2\tau_1} + \omega_0\right)\Delta\tau_1 \tag{26}$$

and

$$\Delta\varphi_2 = \varphi_2\left(\tau_2 + \Delta\tau_2\right) - \varphi_2\left(\tau_2\right) = \left(-\omega_2 - \frac{\omega_2\Delta\tau_2}{2\tau_2} + \omega_0\right)\Delta\tau_2. \tag{27}$$

Because ω_1 and ω_2 are the angle freqenucy of the BFS, which are far less than the light frequency ω_0, both of the first and second term can be ignored. We can see that the phase information in each channel can be independently carried by different frequency components of the BFS. The timing jitter siganls of $\Delta\tau_1$ and $\Delta\tau_2$ induced by the ultrasound signal in channel 1 and channel 2 can be separately obtained by the phase changes of $\Delta\varphi_1$ and $\Delta\varphi_2$, which can be simply expressed by:

$$\Delta\tau_1 \approx \Delta\varphi_1 / \omega_0 \tag{28}$$

and

$$\Delta\tau_2 \approx \Delta\varphi_2 / \omega_0. \tag{29}$$

Thus, the ultrasound signal under test is converted to the timing jitter induced in multiple channel, which can be independently extracted by using the above equations.

In addition, pertaining to the NWDFE, there are still interesting attempts in simplifying the implementation complexity and enhance the performance of the nonlinear equalization in a LED-based UWOC system in **Chapter 3**. For simplicity, the sparsity of linear and nonlinear responses in the UWOC system permits the adoption of only the most significant kernels, enabling the discarding of less important ones for equalization. By maintaining the reliability block and a use block, and rewrite $y(n) = \mathbf{h}^T\mathbf{x}_n = \mathbf{x}_n^T\mathbf{h}$ as a matrix form, the application of the orthogonal matching pursuit (OMP) algorithm during the training phase, resulting in a substantial reduction in the number of kernels.

References

[1] R. I. Network, “Underwater Wireless Communication (UWC) market size: Future growth analysis 2031,” LinkedIn, https://www.linkedin.com/pulse/underwater-wireless-communication-uwc-2f (accessed Jan. 25, 2024).

[2] I. F. Akyildiz, D. Pompili, and T. Melodia, “Underwater acoustic sensor networks: research challenges,” Ad Hoc Netw., vol. 3, no. 3, pp. 257–279, 2005.

[3] M. A. Khalighi, H. Akhouayri, and S. Hranilovic, “Silicon-Photomultiplier-Based Underwater Wireless Optical Communication Using Pulse-Amplitude Modulation,” IEEE J. Ocean. Eng., vol. 45, no. 4, pp. 1611–1621, Oct. 2020.

[4] X. Che, I. Wells, G. Dickers, P. Kear, and X. Gong, “Re-evaluation of RF electromagnetic communication in underwater sensor networks,” IEEE Commun. Mag., vol. 48, no. 12, pp. 143–151, Dec. 2010.

[5] G. Singh and M. Kumar, “Performance analysis of electromagnetic (EM) wave in sea water medium,” Wireless Netw., vol. 26, no. 3, pp. 2125–2135, 2020.

[6] N. Saeed, A. Celik, T. Y. Al-Naffouri, and M.-S. Alouini, “Underwater optical wireless communications, networking, and localization: A survey,” Ad Hoc Netw., vol. 94, p. 101935, 2019.

[7] Z. Zeng, S. Fu, H. Zhang, Y. Dong, and J. Cheng, “A survey of underwater optical wireless communications,” IEEE Commun. Surveys Tuts., vol. 19, no. 1, pp. 204–238, 1st Quart., 2016.

[8] M. F. Ali, D. N. K. Jayakody, and Y. Li, "Recent Trends in Underwater Visible Light Communication (UVLC) Systems," IEEE Access, vol. 10, pp. 22169-22225, 2022.

[9] M. Stojanovic, “Recent advances in high-speed underwater acoustic communications,” IEEE J. Ocean. Eng., vol. 21, no. 2, pp. 125–136, 1996.

[10] R. Diamant and L. Lampe, "Low probability of detection for underwater acoustic communication: A review," *IEEE Access*, vol. 6, pp. 19099-19112, 2018.

[11] R. Diamant, "Choosing the right signal: Doppler shift estimation for underwater acoustic signals," IEEE Journal of Oceanic Engineering, vol. 37, no. 4, pp. 401-410, 2012.

[12] R. Zhang, "A modulation recognition system for underwater acoustic communication signals based on higher-order cumulants and deep learning," *IEEE Journal of Oceanic Engineering*, early access, 2023.

[13] A. K. Das, "Image transmission in underwater acoustic communication channel using LDPC codes," *IEEE Communications Letters*, vol. 27, no. 3, pp. 520-524, 2023.

[14] R. Xing, "Performance analysis of a WPCN-based underwater acoustic communication system," *IEEE Transactions on Wireless Communications*, vol. 22, no. 3, pp. 1761-1771, 2023.

[15] W. Jiang, "Sparse channel estimation for long range underwater acoustic communication," *IEEE Communications Letters*, vol. 26, no. 4, pp. 652-656, 2022.

[16] Y. Lu, "Spatial-digital joint self-interference cancellation method for in-band full-duplex underwater acoustic communication," *IEEE Access*, vol. 10, pp. 117174-117183, 2022.

[17] M. Chen, W. Xu, D. Wang, and L. Wang, "Multi-carrier chaotic communication scheme for underwater acoustic communications," IET Commun., vol. 13, no. 14, pp. 2097–2105, 2019.

[18] T. Ebihara, H. Ogasawara, and G. Leus, "Underwater Acoustic Communication Using Multiple-Input-Multiple-Output Doppler-Resilient Orthogonal Signal Division Multiplexing," IEEE J. Ocean. Eng., vol. 45, no. 4, pp. 1594–1610, 2020.

[19] J. Xi, S. Yan, L. Xu, Z. Zhang, and D. Zeng, "Frequency-Time Domain Turbo Equalization for Underwater Acoustic Communications," IEEE J. Ocean. Eng., vol. 45, no. 2, pp. 665–679, 2020.

[20] X. Cui, P. Yan, J. Li, H. Zhang, S. Li, and J. Liu, "Timing estimation of multiple hyperbolic frequency-modulated signals based on multicarrier underwater acoustic communication," Trans. Emerg. Telecommun. Technol., vol. 33, no. 12, 2022

[21] H. H. Zuberi, S. Liu, M. Z. Sohail, and C. Pan, "Multi-user underwater acoustic communication using binary phase-coded hyperbolic frequency-modulated signals," IET Commun., vol. 16, no. 12, pp. 1415–1427, 2022.

[22] A. Kumar, "A new optimized least-square sparse channel estimation scheme for underwater acoustic communication," Int. J. Commun. Syst., vol. 36, no. 6, 2023.

[23] A. Amantayeva, M. Yerzhanova, and R. C. Kizilirmak, "Multiuser MIMO for underwater visible light communication," Proc. Int. Conf. Comput. Netw. Commun. (CoCoNet), pp. 164-168, Aug. 2018.

[24] Q. Peng, G. Chen, X. Li, Q. Liao, and Y. Guo, “Performance Improvement of Underwater Continuous-Variable Quantum Key Distribution via Photon Subtraction,” Entropy, vol. 21, no. 10, p. 1011, 2019.

[25] J. Xu et al., “OFDM-based broadband underwater wireless optical communication system using a compact blue LED,” Opt. Commun., vol. 369, pp. 100–105, 2016.

[26] F. Hanson and S. Radic, “High bandwidth underwater optical communication,” Appl. Opt., vol. 47, no. 2, pp. 277–283, 2008.

[27] S. Arnon, “Underwater optical wireless communication network,” Opt. Eng., vol. 49, no. 1, pp. 015001–015001, 2010.

[28] M. Doniec, M. Angermann, and D. Rus, “An End-to-End Signal Strength Model for Underwater Optical Communications,” IEEE J. Ocean. Eng., vol. 38, no. 4, pp. 743–757, 2013.
[29] J. S. Jaffe, “Underwater Optical Imaging: The Past, the Present, and the Prospects,” IEEE J. Ocean. Eng., vol. 40, no. 3, pp. 683–700, 2015.

[30] D. Anguita, D. Brizzolara, and G. Parodi, “Optical communication for Underwater Wireless Sensor Networks: a VHDL-implementation of a Physical Layer 802.15.4 compatible,” in OCEANS 2009-EUROPE, 2009.

[31] Y. Dai, X. Chen, X. Yang, Z. Tong, Z. Du, W. Lyu, C. Zhang, H. Zhang, H. Zou, Y. Cheng, D. Ma, J. Zhao, Z. Zhang, and J. Xu, "200-m/500-Mbps underwater wireless optical communication system utilizing a sparse nonlinear equalizer with a variable step size generalized orthogonal matching pursuit," Optics Express, vol. 29, no. 20, pp. 32228-32243, 2021.

[32] C. Fei, Y. Wang, J. Du, R. Chen, N. Lv, G. Zhang, J. Tian, X. Hong, and S. He, "100-m/3-Gbps underwater wireless optical transmission using a wideband photomultiplier tube (PMT)," Opt. Express, vol. 30, pp. 2326-2337, 2022.

[33] C. H. Kang, A. Trichili, O. Alkhazragi, H. Zhang, R. C. Subedi, Y. Guo, S. Mitra, C. Shen, I. S. Roqan, T. K. Ng, M.-S. Alouini, and B. S. Ooi, "Ultraviolet-to-blue color-converting

scintillating-fibers photoreceiver for 375-nm laser-based underwater wireless optical communication," Opt. Express, vol. 27, pp. 30450-30461, 2019.

[34] M. Kong, B. Sun, R. Sarwar, J. Shen, Y. Chen, F. Qu, J. Han, J. Chen, H. Qin, and J. Xu, "Underwater wireless optical communication using a lens-free solar panel receiver," Opt. Commun., vol. 426, pp. 94-98, 2018.

[35] I.-C. Lu and Y.-L. Liu, “205 Mb/s LED-Based Underwater Optical Communication Employing OFDM Modulation,” in 2018 OCEANS - MTS/IEEE Kobe Techno-Oceans (OTO), 2018.

[36] P. Wang, C. Li, and Z. Xu, “A Cost-Efficient Real-Time 25 Mb/s System for LED-UOWC: Design, Channel Coding, FPGA Implementation, and Characterization,” J. Lightw. Technol., vol. 36, no. 13, pp. 2627–2637, 2018.

[37] C. Wang, H.-Y. Yu, Y.-J. Zhu, T. Wang, and Y.-W. Ji, “Multi-LED parallel transmission for long distance underwater VLC system with one SPAD receiver,” Opt. Commun., vol. 410, pp. 889–895, 2018.

[38] N. Chi, Y. Zhao, M. Shi, P. Zou, and X. Lu, “Gaussian kernel-aided deep neural network equalizer utilized in underwater PAM8 visible light communication system,” Opt. Express, vol. 26, no. 20, pp. 26700–26712, 2018.

[39] J. Li, F. Wang, M. Zhao, F. Jiang, and N. Chi, “Large-coverage underwater visible light communication system based on blue LED employing equal gain combining with integrated PIN array reception,” Appl. Opt., vol. 58, no. 2, pp. 383–388, 2019.

[40] Y. Zhou et al., “Common-anode LED on a Si substrate for beyond 15 Gbit/s underwater visible light communication,” Photon. Res., vol. 7, no. 9, p. 1019, 2019.

[41] G. Stepniak, J. Siuzdak, and P. Zwierko, “Compensation of a VLC Phosphorescent White LED Nonlinearity by Means of Volterra DFE,” IEEE Photon. Technol. Lett., vol. 25, no. 16, pp. 1597–1600, 2013.

[42] C. Fei et al., "Underwater wireless optical communication utilizing low-complexity sparse pruned-term based nonlinear decision-feedback equalization," Appl. Opt., vol. 61, no. 22, pp. 6534-6543, Aug. 2022.

[43] Y. Wang, L. Tao, X. Huang, J. Shi, and N. Chi, "Enhanced Performance of a High-Speed WDM CAP64 VLC System Employing Volterra Series-Based Nonlinear Equalizer," IEEE Photon. J., vol. 7, no. 3, pp. 7901907, June 2015.

[44] Y. Zhou, J. Zhang, C. Lu, and C. Guo, "Low-Complexity Frequency-Domain Nonlinear Equalizer with Absolute Operation for Underwater Wireless Optical Communications," Opt. Express, vol. 31, no. 14, pp. 23086-23094, June 2023.

[45] C. Fei, J. Zhang, G. Zhang, Y. Wu, X. Hong, and S. He, "Demonstration of 15-m 7.33-Gb/s 450-nm underwater wireless optical discrete multitone transmission using post nonlinear equalization," J. Lightwave Technol., vol. 36, no. 4, pp. 728-734, Feb. 2018.

[46] G. Zhang, J. Zhang, and S. He, "Low-complexity frequency-domain nonlinear equalizer for underwater wireless optical communications," IEEE J. Oceanic Eng., vol. 43, no. 3, pp. 640-650, Jul. 2018.

[47] G. Zhang, C. Fei, S. He, and X. Hong, "Sparse nonlinear equalization with match pursuit for LED based visible light communication systems," in Proc. Asia Commun. Photonics Conf. (ACP), 2017, pp. 1-3.

[48] S. D. Murugan, S. S. Iyer, and A. M. Fardad, "High-Speed Underwater Optical Wireless Communication Systems: A Survey," IEEE Access, vol. 9, pp. 10921-10934, Jan. 2021.

[49] Z. Wang, H. Zhang, and J. Li, "200-m/500-Mbps underwater wireless optical communication system utilizing a sparse nonlinear equalizer," IEEE Photonics Technol. Lett., vol. 33, no. 6, pp. 267-270, Mar. 2021.

[50] L. Guoqiang, W. Chaofan, L. Zhongya, Z. Peng, H. Fangchen, and C. Nan, "Application of neural network based post equalization methods in underwater visible light communication," J. Commun. Univ. China (Sci. Technol.), vol. 28, no. 2, pp. 61-68, Apr. 2021.

[51] H. Zhang, Y. Liu, and P. Wang, "High-Speed Underwater Optical Wireless Communication: From a Perspective of Advanced Modulation Formats," IEEE J. Sel. Areas Commun., vol. 39, no. 5, pp. 1107-1120, May 2021.

[52] Y. Wu, C. Fei, and S. He, "Sparse nonlinear equalization for underwater wireless optical communications," IEEE Trans. Wireless Commun., vol. 18, no. 8, pp. 4240-4252, Aug. 2019.
[53] X. Chen, Q. Zhang, and Y. Huang, "90-m/660-Mbps underwater wireless optical communication enabled by interleaved single-carrier FDM scheme combined with sparse

weight-initiated DNN equalizer," J. Lightwave Technol., vol. 39, no. 16, pp. 5310-5317, Aug. 2021.

[54] G. Stepniak, J. Siuzdak, and P. Zwierko, "Compensation of a VLC phosphorescent white LED nonlinearity by means of Volterra DFE," IEEE Photon. Technol. Lett., vol. 25, no. 16, pp. 1597-1600, Aug. 2013.

[55] Y. Wang, L. Tao, X. Huang, J. Shi, and N. Chi, "Enhanced performance of a high-Speed WDM CAP64 VLC system employing Volterra series-based nonlinear equalizer," IEEE Photon. J., vol. 7, no. 4, pp. 1-7, Aug. 2015.

[56] J. Li, Z. Huang, X. Liu, and Y. Ji, "Hybrid time-frequency domain equalization for LED nonlinearity mitigation in OFDM-based VLC systems," Opt. Express, vol. 23, no. 1, pp. 611-619, Jan. 2015.

[57] G. Zhang, C. Fei, S. He, and X. Hong, "Sparse nonlinear equalization with match pursuit for LED based visible light communication systems," in Proc. Asia Commun. Photonics Conf. (ACP), 2017, pp. 1-3.

[58] T. Kamalakis, J. W. Walewski, G. Ntogari, and G. Mileounis, "Empirical Volterra-series modeling of commercial light-emitting diodes," J. Lightwave Technol., vol. 29, no. 14, pp. 2146-2155, Jul. 2011.

[59] H. Zhou, M. Zhang, X. Wang, and X. Ren, “Design and Implementation of more than 50m Real-Time Underwater Wireless Optical Communication System,” J. Lightw. Technol., vol. 40, no. 12, pp. 3654–3668, June 2022.

[60] G. Qiao, Z. Babar, L. Ma, S. Liu, and J. Wu, “MIMO-OFDM underwater acoustic communication systems—A review,” Phys. Commun., vol. 23, pp. 56–64, 2017.

[61] Y. Zhou, Y. Li, Y.-C. He, X. Wang, and M. Yu, “Artificial fish swarm based power allocation algorithm for MIMO-OFDM relay underwater acoustic communication,” IET Commun., vol. 12, no. 9, pp. 1079–1085, 2018.

[62] M. J. Bocus, A. Doufexi, and D. Agrafiotis, “Performance of OFDM-based massive MIMO OTFS systems for underwater acoustic communication,” IET Commun., vol. 14, no. 4, pp. 588–593, 2020.

[63] G. Wissmeyer, M. A. Pleitez, A. Rosenthal, et al., “Looking at sound: optoacoustics with all-optical ultrasound detection,” Light: Sci. Appl., vol. 7, no. 1, p. 53, 2018.

[64] S. Liang, S. C. Tjin, B. Lin, et al., “Novel fiber Bragg grating sensing method based on the sidelobe modulation for ultrasound detection,” J. Lightw. Technol., vol. 37, no. 11, pp. 2686–2693, 2018.

[65] L. Yang, D. Xu, G. Chen, et al., “Miniaturized fiber optic ultrasound sensor with multiplexing for photoacoustic imaging,” Photoacoustics, vol. 28, p. 100421, 2022.

[66] M. A. Cutolo and G. Breglio, “Interferometric Fabry-Perot sensors for ultrasound detection on the tip of an optical fiber,” Results Opt., vol. 6, p. 100209, 2022.
[67] T. Ling, S. L. Chen, and L. J. Guo, “Fabrication and characterization of high Q polymer micro-ring resonator and its application as a sensitive ultrasonic detector,” Opt. Express, vol. 19, no. 2, pp. 861–869, 2011.

[68] F. Xu, J. Shi, K. Gong, et al., “Fiber-optic acoustic pressure sensor based on large-area nanolayer silver diaphragm,” Opt. Lett., vol. 39, no. 10, pp. 2838–2840, 2014.

[69] J. Bauer-Marschallinger, K. Felbermayer, and T. Berer, "All-optical photoacoustic projection imaging," Biomed. Opt. Express, vol. 8, no. 9, pp. 3938-3951, 2017.

[70] H. Liu, Y. Wu, C. Hou, et al., "Ultrasound pulse generation through continuous-wave laser excited thermo-cavitation for all-optical ultrasound imaging," APL Photonics, vol. 8, no. 4, pp. 1-7, 2023.

[71] L. Yang, Y. Li, F. Fang, et al., "Highly sensitive and miniature microfiber-based ultrasound sensor for photoacoustic tomography," Opto-Electron. Adv., vol. 5, no. 6, pp. 200076-1-200076-8, 2022.

[72] Y. Zhang, Y. Liang, L. Jin, et al., "125 μm fiber based all-optical ultrasound probes for pulse-echo imaging," Chin. Opt. Lett., vol. 17, no. 7, pp. 070604-1, 2019.

[73] X. Zhong, Y. Liang, X. Wang, et al., "Free-moving-state microscopic imaging of cerebral oxygenation and hemodynamics with a photoacoustic fiberscope," Light: Sci. Appl., vol. 13, no. 1, pp. 5-5, 2024.

[74] Y. Tong, X. Guo, M. Li, et al., "Ultrafast optical phase-sensitive ultrasonic detection via dual-comb multiheterodyne interferometry," Adv. Photon. Nexus, vol. 2, no. 1, pp. 016002-1-016002-2, 2023.

[75] J. Pan, Q. Li, Y. Feng, et al., "Parallel interrogation of the chalcogenide-based micro-ring sensor array for photoacoustic tomography," Nat. Commun., vol. 14, no. 1, pp. 3250-3250, 2023.

[76] A. Mahjoubfar, D. V. Churkin, S. Barland, et al., "Time stretch and its applications," Nat. Photon., vol. 11, no. 6, pp. 341-351, 2017.

[77] J. L. Wu, Y. Q. Xu, J. J. Xu, et al., "Ultrafast laser-scanning time-stretch imaging at visible wavelengths," Light: Sci. Appl., vol. 6, no. 1, pp. e16196, 2017.

[78] K. Goda and B. Jalali, "Dispersive Fourier transformation for fast continuous single-shot measurements," Nat. Photon., vol. 7, no. 2, pp. 102-112, 2013.

[79] H. Chen, Y. Li, D. Huang, et al., "114 nm broadband all-fiber nonlinear polarization rotation mode locked-laser and time-stretch optical coherence tomography," Opt. Express, vol. 29, no. 21, pp. 33322-33330, 2021.

[80] D. Huang, F. Li, Z. He, et al., "400 MHz ultrafast optical coherence tomography," Opt. Lett., vol. 45, no. 24, pp. 6675-6678, 2020.

[81] Z. Zeng, S. Fu, H. Zhang, Y. Dong, and J. Cheng, "A Survey of Underwater Optical Wireless Communications," IEEE Commun. Surv. & Tut., vol. 19, no. 1, pp. 204-238, 2017.

[82] N. Saeed, A. Celik, T. Y. Al-Naffouri, and M.-S. Alouini, "Underwater optical wireless communications, networking, and localization: A survey," Ad Hoc Netw., vol. 94, p. 101935, 2019.

[83] J. Xu, "Underwater wireless optical communication: Why, what, and how? [Invited]," Chin. Opt. Lett., vol. 17, no. 10, pp. 100007-1, 2019.

[84] X. Yang et al., "7-M/130-Mbps LED-to-LED underwater wireless optical communication based on arrays of series-connected LEDs and a coaxial lens group," J. Lightw. Technol., vol. 40, no. 17, pp. 5901-5909, Sep. 2022.

[85] E. F. Schubert, N. Hunt, R. J. Malik, M. Micovic, and D. L. Miller, "Temperature and modulation characteristics of resonant-cavity light-emitting diodes," J. Lightw. Technol., vol. 14, no. 7, pp. 1721-1729, Jul. 1996.

[86] T. Kamalakis, J. W. Walewski, G. Ntogari, and G. Mileounis, "Empirical Volterra-Series Modeling of Commercial Light-Emitting Diodes," J. Lightw. Technol., vol. 29, no. 14, pp. 2146-2155, Jul. 2011.

[87] R. Rath, D. Clausen, S. Ohlendorf, S. Pachnicke, and W. Rosenkranz, "Tomlinson–Harashima Precoding For Dispersion Uncompensated PAM-4 Transmission With Direct-Detection," J. Lightw. Technol., vol. 35, no. 18, pp. 3909-3917, Sep. 2017.

[88] W. Niu et al., "Neural-Network-Based Nonlinear Tomlinson-Harashima Precoding for Bandwidth-Limited Underwater Visible Light Communication," J. Lightw. Technol., vol. 40, no. 8, pp. 2296-2306, Apr. 2022.

[89] J. Zhang et al., "C-band 120-Gb/s PAM-4 transmission over 50-km SSMF with improved weighted decision-feedback equalizer," Opt. Express, vol. 29, no. 25, pp. 41622-41633, Nov. 2021.

[90] J. Zhang et al., "Improved Weighted Volterra DFE for C-Band 100-Gbit/s PAM-4 Transmission over 60-km SSMF," IEEE Photon. Technol. Lett., vol. 35, no. 4, pp. 163-166, Feb. 2023.